Non-stem progenitors enable coordinated changes in gut epithelial cell-type composition

Laura E. Sanman[1]†, Ina W. Chen[1]†, Jake M. Bieber[1,2], Veronica Steri[3,4], Byron Hann[3,4], Lani F. Wu[1]*, Steven J. Altschuler[1]*

[1]Department of Pharmaceutical Chemistry, University of California San Francisco, San Francisco, CA 94158, USA

[2]Graduate Program in Bioengineering, University of California Berkeley, Berkeley CA 94720, USA

[3]Helen Diller Family Comprehensive Cancer Center, University of California, San Francisco, San Francisco, CA 94158, USA.

[4]Preclinical Therapeutics Core, University of California, San Francisco, San Francisco, CA 94158, USA.

*Correspondence to: lani.wu@ucsf.edu, steven.altschuler@ucsf.edu

†Equal contributions

Abstract

Renewing tissues have the remarkable ability to maintain both proliferative progenitor and specialized mature cell types at consistent ratios. How are complex milieus of microenvironmental signals interpreted to coordinate tissue cell-type composition? Here, we develop a high-throughput approach, combining organoid technology, combinatorial perturbations, and quantitative imaging to address these questions in the context of the intestinal epithelium. We find that changes in proliferation of transit-amplifying (TA) cells, but not Lgr5$^+$ stem cells, alters the composition of mature secretory and absorptive cell-types in organoids and *in vivo*. The link between TA proliferation and mature fate bias arises from differential amplification of secretory and absorptive progenitor cells. Further, TA cells have a distinct pattern of regulation from other epithelial cell-types that stems, in part, from signal integration via the MEK-Erk pathway and paracrine BMP production. These results demonstrate that TA cells, a feature of many renewing tissues, play a critical role in converting complex microenvironmental signals into changes in cell-type composition.

Introduction

A central question in the study of complex tissues is how diverse signals are integrated to give rise to changes in a tissue's cell-type composition. This is a particularly challenging question to answer due to the plethora of tissue-intrinsic and microenvironmental signals that influence cell fate decision-making in progenitor cells. In many tissues, this question is further complicated by the existence of both stem and transit-amplifying (TA) progenitors. What are the signaling networks that integrate the complex milieu of microenvironmental signals? Do stem and TA cells play different roles in shaping the cell-type composition of the tissue?

Here, we address these questions in the context of the intestinal epithelium, a model renewing tissue[1,2,3]. Our approach builds on a previously established enteroid monolayer culture system that recapitulates key properties of the intestinal epithelium and is amenable to quantitative microscopy due to its 2D nature[4]. We combine enteroid culture with high-throughput combinatorial perturbation and quantitative imaging of stem, TA, and differentiated cell-types. We develop analytical frameworks to analyze the resulting data (single and combinatorial perturbations x multiple cell-types), enabling us to characterize networks of signaling crosstalk that give rise to each epithelial cell-type and discern how stem and transit-amplifying progenitors shape gut epithelial cell-type composition. While enteroid monolayers are used as a primary platform, key observations are evaluated in 3D organoids and *in vivo*.[2]

Our analysis reveals two principles underlying the regulation of the intestinal epithelium. First, we find that proliferation of TA cells, but surprisingly not Lgr5$^+$ stem cells, regulates the composition of mature cell-types in the intestinal epithelium. Specifically, inhibiting TA proliferation increases secretory cell abundance. We observe this connection between proliferation and secretory cells in enteroid monolayers, 3D organoids, and mice. Modeling and experimental evidence suggest that this anticorrelation is due to decreased amplification of secretory progenitors relative to other (absorptive) progenitors. These data suggest a key role for TA cells, an often-overlooked cell population, in coordinating tissue cell-type composition. Second, we find that distinct networks of signaling crosstalk shape the prevalence of each cell-type, with a unique pattern of crosstalk regulating TA cell abundance. Our analysis identified novel crosstalk between EGFR, BMP, and IL-4 pathway modulators that regulates TA proliferation, leading us to find that signals can be integrated at both the signaling pathway level (MEK-Erk) and at the tissue level, via induction of secondary mediators (BMPs). This study reveals principles underlying regulation of the intestinal epithelium and, more broadly, establishes a generalizable approach for studying signaling crosstalk and coordinated decision-making in complex tissues.

Results

A quantitative microscopy platform to study tissue cell-type composition

During renewal of the intestinal epithelium, proliferating Lgr5$^+$ crypt-base stem cells differentiate into proliferating TA progenitors, which in turn adopt absorptive (enterocyte) or secretory (Paneth, goblet, enteroendocrine) cell fates[1] (Fig. 1a). To understand how combinations of microenvironmental signals are interpreted to regulate tissue cell-type composition, we made use of a recently developed enteroid monolayer culture system. These cultures recapitulate key features of the intestinal epithelium including representation of each major intestinal epithelial cell-type (Lgr5$^+$ stem, transit-amplifying, and differentiated secretory and absorptive cells), apical-basolateral polarization, and self-organization[4]. Importantly, enteroid monolayers can be systematically perturbed and assayed via imaging.

To interrogate diverse epithelial cell-types, algorithms were developed that accurately quantify the numbers of cells expressing markers of progenitor (Lgr5$^+$ stem and EdU$^+$ proliferating) and mature specialized (Lyz$^+$ Paneth, Muc2$^+$ goblet, and ChgA$^+$ enteroendocrine (EE)) cells in images of enteroid monolayers (Supplementary Fig. 1, Supplementary Table 1). Measurements of individual cell-type numbers were combined into readouts of progenitor cell proliferation and mature cell-fate specification (Fig. 1b, Supplementary Fig. 1). To measure stem and transit-amplifying (TA) cell proliferation, the number of EdU$^+$ Lgr5$^+$ and EdU$^+$ Lgr5$^-$ cells were quantified, respectively (specific TA markers are lacking, thus TA cells were defined as non-stem proliferating cells). To measure the secretory-absorptive cell-fate decision, the fraction of differentiated (Lgr5$^-$ EdU$^-$) cells that express secretory (Paneth, goblet, enteroendocrine) markers was quantified (#secretory/#diff). This is a reasonable approximation as Paneth, goblet, and EE cells make up the majority of secretory cells; the remaining differentiated cells are of the absorptive lineage[1,5]. Finally, to capture biases towards each cell-type within the secretory lineage, the specific fraction of all secretory cells positive for Paneth (Lyz), goblet (Muc2), and EE (ChgA) cell markers was quantified (#Paneth/#secretory, #goblet/#secretory, #EE/#secretory). Quantifying the fractions of mature cell-types within differentiated cell populations allows cell-fate specification to be studied independently of changes in the overall number of differentiated cells, which can be altered by changes in the relative abundance of progenitor and differentiated cells (see Supplementary Discussion).

We next benchmarked our experimental platform for reproducibility and response to well-characterized modulators. First, in the untreated condition (vehicle control), jejunal enteroid monolayers exhibited cell-type composition like that of the *in vivo* small intestinal epithelium (Supplementary Fig. 2, Supplementary Table 2). Cell-type composition after 48 hours of culture was consistent when monolayers were initially seeded between 10-30% confluency, indicating low inter-replicate variability in the chosen cell-type readouts (Supplementary Fig. 2). Second, the responses of enteroid monolayers to established modulators of proliferation (GSK3-i and Wnt3a) and cell-fate specification (Notch-i, IL-4, EGFR-i, PORCN-i) were in agreement with previous studies in 3D organoids and *in vivo*[3,6–10] (Supplementary Fig. 2, Supplementary Table 3). Third, changes in numbers of stem and TA cells and the fractions of goblet and Paneth cells were evident after 48 hours of perturbation (Supplementary Fig. 2). Finally, by performing an EdU pulse-chase experiment, it was observed that after 48 hours, the vast majority (~80%) of cells in enteroid monolayers were produced from the cells that were in S phase upon initial plating (Supplementary Fig. 2). These data, coupled with the previous observation that longer (72 hours+) culture times can result in secondary effects of perturbations[4], resulted in the selection of a 48 hour time point for further studies. Taken together, enteroid monolayers respond as expected to well-characterized modulators of cell-type composition, recapitulating morphogen responses previously observed both in 3D organoids and in mice. Further, these data establish a robust workflow for capturing tissue-wide responses to perturbations (Supplementary Fig. 2).

Systematic addition of single and pairwise signaling molecules reveals cell-type-specific regulators

To comprehensively elucidate regulation of progenitor proliferation and mature cell-fate specification, 13 epithelial-intrinsic and microenvironmental modulators that target 8 core intestinal epithelial signaling pathways (Wnt, BMP, Notch, HDAC, JAK, p38MAPK, TGF-β, EGFR[6,8,11–15]) and are known to have diverse effects on tissue cell-type composition were selected (Supplementary Table 3). These modulators were applied to enteroid monolayers singly (13 conditions) and in all possible pairwise combinations (78 conditions), using concentrations suggested by literature reports and confirmed by dose-response experiments (Supplementary Fig. 3, Supplementary Table 3, Supplementary Methods)[6–8]. Effects on numbers of EdU$^+$ stem and TA cells as well as fractions of secretory, Paneth, goblet, and EE cells were measured as described above (Fig. 1c, Supplementary Fig. 1, Supplementary Fig. 4). The number of nuclei per well was also measured (Supplementary Fig. 4). The vast majority of the 546 perturbation effects (91 conditions x 6 cell-type features)—beyond those used for benchmarks with past work—were previously uncharacterized (Fig. 1c, Supplementary Fig. 4).

Analysis of both single and combinatorial perturbation phenotypes revealed new regulatory effects. For example, TGF-β treatment resulted in a surprising decrease in the fraction of secretory cells (Fig. 1d, #secretory/#diff). GSK3-i and JAK1/2-i synergistically increased stem cell proliferation, inducing a 5-fold increase in #EdU$^+$ stem cells, which was more than the 4-fold increase in #EdU$^+$ stem cells induced by the current benchmark GSK3-i+HDAC-i[6] (Fig. 1e). Finally, conditions were identified that selectively enrich for EE cells, notably TGF-β+PORCN-i, which increased EE cell abundance relative to other secretory cell-types >2-fold more strongly than current benchmarks (7-fold compared to ~3-fold with pairwise combinations of EGFR-i, PORCN-i, Notch-i[8]; Fig. 1f). Notably, these effects were recapitulated in 3D organoid cultures (Fig. 1d-f, images), indicating that responses to signaling modulators are conserved across epithelial culture systems, even with a lack of 3D tissue architecture[4]. More broadly, striking differences in the regulation of EdU$^+$ stem and TA cells were observed; combinations of TGF-βR-i, JAK1/2-i, GSK3-i, and p38 MAPK-i increased #EdU$^+$ stem cells but not #TA cells (Fig. 1c, callout 1), whereas Wnt3a combinations increased #TA cells but not #EdU$^+$ stem cells (Fig. 1c, callout 2). These data indicated that stem and TA cells have distinct regulatory and signal integration properties.

Transit-amplifying cell proliferation alters secretory cell-fate specification

What are the relative roles of stem and TA cells in regulating cell-type composition? To address this question, it was examined whether stem and TA abundances correlated with any readouts of cell-fate specification, indicating potential co-regulation. First, correlations between readouts of proliferation and cell-fate specification were evaluated (Fig. 2a, left scatterplots), using the single and combinatorial perturbation data described above. Second, to assess whether cell-type correlations were driven by individual pathways, perturbations were systematically dropped from the dataset and correlations re-examined (Fig. 2a, ‘leave-one-out’).

There was little-to-no correlation between the number of proliferating Lgr5$^+$ stem cells and any marker of mature cell-fate specification (Fig. 2a, left scatterplots). In contrast, a connection between transit-amplifying cell numbers and cell-fate specification was apparent. Specifically, as the number of transit-amplifying cells increased, both the overall fraction of differentiated cells expressing secretory markers and the specific fraction of secretory cells expressing EE cell markers decreased (Fig. 2a, middle scatterplots). We noted that dropping EGFR-i from the dataset largely abrogated the anticorrelation between TA and EE cells (Fig 2a, red arrowhead), which is consistent with recent work suggesting that EE cell production can be triggered by EGFR-i-induced stem cell quiescence[8]. Yet, the correlation between TA and secretory cells was maintained even when systematically dropping perturbations from the dataset, indicating that the correlation is driven by diverse morphogenic factors (Fig. 2a, right, ‘leave-one-out’). Intriguingly, altering proliferation directly, rather than targeting a specific morphogenic pathway, was sufficient to alter secretory cell specification: Cdk and Aurora kinase inhibitors decreased EdU$^+$ stem cell and TA cell numbers while increasing secretory cell fractions (Fig. 2b).

Since both stem and TA cells are present in enteroid cultures, it is difficult to disentangle the role of each progenitor type in driving the correlation between proliferation and secretory cell fractions. To determine if stem or TA cells are responsible for the correlation, responses to MEK or CDK4/6 inhibitors, both of which significantly impair proliferation in intestinal organoids[9], were compared over time for high-purity 3D organoid cultures of stem (enriched for Lgr5$^+$ cells, derived by treating with GSK3-i+HDAC-i[6]) or TA (depleted for Lgr5$^+$ cells, derived by treating for 1 day with PORCN-i) cells. Atoh1 and Hes1 RNA levels were measured by qPCR to quantify changes in secretory and absorptive cell fractions, respectively. Strikingly, MEK and CDK4/6 inhibition increased the ratio of Atoh1/Hes1 RNA in 3D cultures of TA cells, but not in 3D cultures of Lgr5$^+$ stem cells (Fig. 2c). These data indicate that signal processing in TA cells themselves, but not in Lgr5$^+$ stem cells, is sufficient to drive coordination of TA cell numbers with secretory cell-fate specification.

How does altering TA cell proliferation affect the abundance of secretory cells relative to other differentiated (absorptive) cell-types? Previous studies showed that commitment to a secretory fate (in that case, expression of the Notch ligand Dll1) is coincident in time with cell cycle exit[16], and that secretory cell clones resulting from lineage tracing are smaller on average than absorptive cell clones[17]. Therefore, a potential explanation for why inhibiting cell cycling increased the relative abundance of secretory cells is that secretory progenitors undergo fewer rounds of division than absorptive progenitors. To mathematically evaluate this hypothesis, a simple exponential growth model was established to simulate how the secretory:absorptive ratio changes when varying division rates for secretory and absorptive progenitors (Supplementary Methods). Only under conditions where secretory progenitors divide fewer times than absorptive progenitors did the model recapitulate the observed trend of the effect of cell cycle modulation on the ratio of secretory:absorptive cells (Fig. 2d, Supplementary Fig. 5). To experimentally test this hypothesis, an EdU dilution experiment was conducted. A pulse of EdU was administered for the first 9 hours of culture (less than one TA cell cycle length[18]), followed by a chase of 48 hours. Cells were fixed and stained with fluorophore-conjugated UEA1, a lectin that binds to goblet and Paneth cells[19], and EdU signal measured both in all cells and UEA1+ cells. Importantly, goblet and Paneth cells comprise the majority of secretory cells (Supplementary Fig. 2). EdU signal was less diluted in UEA1+ cells than in all cells (Fig. 2e), indicating that UEA1$^+$ subpopulation of secretory cells divided fewer times than the overall population of intestinal epithelial cells.

To assess whether the relationship between proliferation and the ratio of secretory:absorptive cells is recapitulated *in vivo*, mice (n=8 per group) were treated with the CDK4/6 inhibitor palbociclib or vehicle. After 50 hours of treatment, intestinal crypts were harvested and gene expression was measured by RT-qPCR. CDK4/6-i treatment decreased Ki67 expression, indicating a decrease in proliferation, and increased the Atoh1/Hes1 ratio, indicating an increase in the secretory-absorptive ratio (Fig. 2f).

TA cells integrate signals via cell-type-specific patterns of crosstalk

How are combinations of signals integrated to regulate TA cell proliferation and thus mature cell-type composition? Though much work has gone into elucidating control of stem cell proliferation[6,8,20], it is less clear how TA cell proliferation is regulated. It was previously observed that, while TA cells have a similar regulatory pattern to stem cells, there were also notable differences (Fig. 1c). To further elucidate how signals are integrated to regulate TA cell numbers in comparison to other cell-types, patterns of crosstalk between signals were examined. For each readout (e.g., #TA cells), crosstalk between the 13 different perturbations was defined analytically as combinatorial perturbation effects that deviated significantly ($p<0.01$) from a multiplicative model[21]. (A linear-fit model[22,23] performed similarly but the multiplicative model was chosen due to its interpretability; Supplementary Fig. 6, Supplementary Discussion). Biologically, crosstalk was interpreted as direct or indirect connections between the perturbed signaling pathways[24,25].

Broadly, distinct patterns of crosstalk regulated the abundance of each cell-type. Extensive crosstalk amongst diverse perturbations regulated EdU$^+$ stem and TA cell numbers, while little crosstalk regulated goblet or Paneth cell fractions (Fig. 3a). Crosstalk amongst perturbations to TGF-β signaling regulated secretory cell fractions (Fig. 3a, starred), consistent with the finding that TGF-β affects the secretory/absorptive cell balance (Fig. 1d). These data indicated that distinct patterns of crosstalk underlie the production of each cell-type and that signal crosstalk influences abundance of progenitor cells more strongly than the process of mature cell-fate-specification.

To further understand how perturbed pathways are connected in TA cells, crosstalk patterns were visualized as a network, with nodes representing perturbations and edges connecting pairs of perturbations that exhibit large deviations (effect size>5) from the multiplicative model. BMP4 was highly connected to this network (Fig. 3b), though less so than in the EdU$^+$ stem cell network (Supplementary Fig. 6), consistent with recent work demonstrating that BMP suppresses stem cell signature genes and, consequently, proliferation[10]. Perturbations targeting the Wnt pathway (Wnt, GSK3-i, PORCN-i) were highly connected in the TA cell network, more so than in the EdU$^+$ stem cell network, consistent with the observation that Wnt3a specifically upregulated TA cells (Fig. 1c, callout 2). Finally, TGF-β and BMP were connected, perhaps due to utilization of similar downstream factors such as SMAD proteins[25].

EGFR-i, IL-4, and BMP crosstalk regulates transit-amplifying cell proliferation via intracellular MEK/Erk signaling and paracrine BMP production

Beyond known or expected connections, the mechanisms underlying several remaining pairwise connections, specifically those involving IL-4, BMP4, and EGFR-i, were previously uncharacterized (Fig. 3b, red edges). The mechanism(s) underlying crosstalk between these pathways were particularly interesting due to the strength of the identified crosstalk and its specificity for regulation of TA cell numbers (Fig. 3a, arrowheads).

IL-4—EGFR-i crosstalk was identified because, while each perturbation decreased proliferation alone, their combined effect was mutually antagonistic (Fig 4a, compare number of EdU$^+$ cells). Though EGFR-i decreases proliferation by reducing MEK-Erk activity[8], IL-4 treatment resulted in MEK-Erk activation (as measured by phospho-Erk nuclear translocation) even in the context of EGFR inhibition (Fig. 4b). This suggested that IL-4 antagonized the effects of EGFR-i by enabling bypass MEK-Erk activation, which is further supported by the observation that IL-4 did not antagonize the effects of EGFR-i (or induce phospho-Erk nuclear translocation) when MEK was inhibited (Fig. 4c, Supplementary Fig. 7). Nuclear phospho-Erk was observed in proliferating cells (CyclinD1$^+$) but not stem (Lgr5$^+$) cells (Supplementary Fig. 7), indicating why crosstalk between these perturbations was specific to TA cells rather than shared with stem cells. Further, by investigating the IL-4—BMPR-i connection, it was observed that IL-4 reduced proliferation in both enteroid monolayers and 3D organoids by increasing the levels of BMP2 (the epithelial paralog of mesenchymal BMP4[26]) produced by the tissue (Fig. 4d, Supplementary Fig. 7). EGFR-i reduced IL-4-induced BMP2 production (Fig. 4e), suggesting a mechanism by which EGFR-i antagonizes the effects of IL-4.

For EGFR-i—BMP4 crosstalk, which also specifically regulated TA cell numbers, combined EGFR-i and BMP4 treatment decreased TA cell numbers similarly to BMP4 treatment alone (Fig. 4f), suggesting shared downstream components[21]. Indeed, crosstalk was also due to shared modulation of the MEK/Erk pathway: while BMP4 treatment did not change Erk phosphorylation significantly (Supplementary Fig. 7), it did decrease Cdk6 expression (Fig. 4g). These data suggested that surprisingly diverse perturbations can be integrated to regulate TA cell numbers by tuning the activity of individual signaling pathways (e.g., MEK-Erk) and production of secondary mediators (e.g., BMPs).

Discussion

For proper tissue renewal to occur, multiple cell-types must concurrently and reproducibly integrate a complex milieu of signals and make coordinated cell-fate decisions. How renewing tissues integrate complex signals to regulate diverse cell fates is poorly understood. A major challenge is that tissues are composed of heterogeneous cellular subtypes, each of which can interpret environmental signals differently and contribute differently to overall tissue responses. The intestinal epithelium is particularly remarkable in that it accurately recapitulates the process of renewal every 3-5 days throughout our lifetimes. Though much progress has been made in defining the ‘parts list’ of factors that guide intestinal epithelial renewal, it was unclear how these factors are integrated—and by which cell-types—to enable diverse cell-fate decisions.

This study presents a systematic and comprehensive interrogation of how microenvironmental signals are integrated by a complex renewing tissue. By introducing combinations of microenvironmental factors, we found that distinct patterns of signaling crosstalk drive the production of each intestinal epithelial cell-type. Notably, there was more extensive crosstalk amongst signals driving progenitor (stem and TA) cell proliferation than specification of mature cell-types. This implies that more signals control progenitor proliferation, or that signals act redundantly upon a smaller number of shared pathways. We focused particularly on elucidating TA cell regulation, which has largely been overlooked by previous studies. Crosstalk regulating TA cell numbers could be attributed to shared utilization of intracellular signaling pathways, such as the MEK/Erk pathway, and co-regulation of paracrine signaling molecules that act extracellularly, such as BMPs. Taken together, these mechanisms of signal integration, which differ by cell-type and can even produce additional secondary mediators, allow different combinations of a core repertoire of microenvironmental factors to generate functional diversity from a population of seemingly homogeneous progenitor cells[27].

The intestinal epithelium, like many tissues, is generated by stem cells that differentiate into TA cells and then assume mature cell fates. Our study points to a pivotal role for the TA population in regulating mature cell-type composition. Specifically, signals that broadly perturbed TA cell proliferation altered the balance of secretory and absorptive cell-types. This property is observed in enteroid monolayers, 3D organoids, and mice. The connection between TA cell proliferation and secretory-absorptive cell fates likely stems from decreased cycling of secretory progenitors relative to absorptive progenitors, which provides a strategy for maintaining the abundance of protective cell-types, such as goblet, Paneth, and enteroendocrine cells, during times of infection, stress, or injury[28]. Intriguingly, many tissues, including the brain, skin, and hematopoietic system, feature transit-amplifying cells as intermediates between the stem and differentiated cell populations. Further, a recent study suggested that myeloid and megakaryocyte progenitors, in contrast to other blood progenitor cells, do not undergo cell division, indicating that the myeloid cells and megakaryocytes would be selected for during times of decreased progenitor proliferation[29]. Thus, proliferating non-stem progenitors may broadly serve as a buffer that enables coordinated tissue responses to a changing microenvironment while insulating the stem cell population from extreme changes.

Acknowledgments

We are grateful to Zev Gartner, Ophir Klein, Curtis Thorne, and members of the Altschuler-Wu lab for their feedback. We additionally thank Ophir Klein and Frederic de Sauvage for mouse resources. This work was supported by NIH GM112690 (S.J.A.), NCI-NIH RO1 CA184984 (L.F.W.), the UCSF Program for Breakthrough Biomedical Research which is partly funded by the Sandler Foundation (L.F.W.), NIH NRSA fellowship F32DK120102 (L.E.S.), and NSF GRFP fellowship 1650113 (I.W.C.).

Author contributions

L.E.S. and I.W.C. conceptualized study, developed computational methods, designed and executed experiments, analyzed data, and wrote the manuscript. J.M.B. and V.S. designed and executed in vivo experiments and analyzed data. B.H. supervised the in vivo study. L.F.W. and S.J.A. conceptualized and supervised the overall study and wrote the manuscript.

Competing interests

Authors declare no competing interests.

Figures

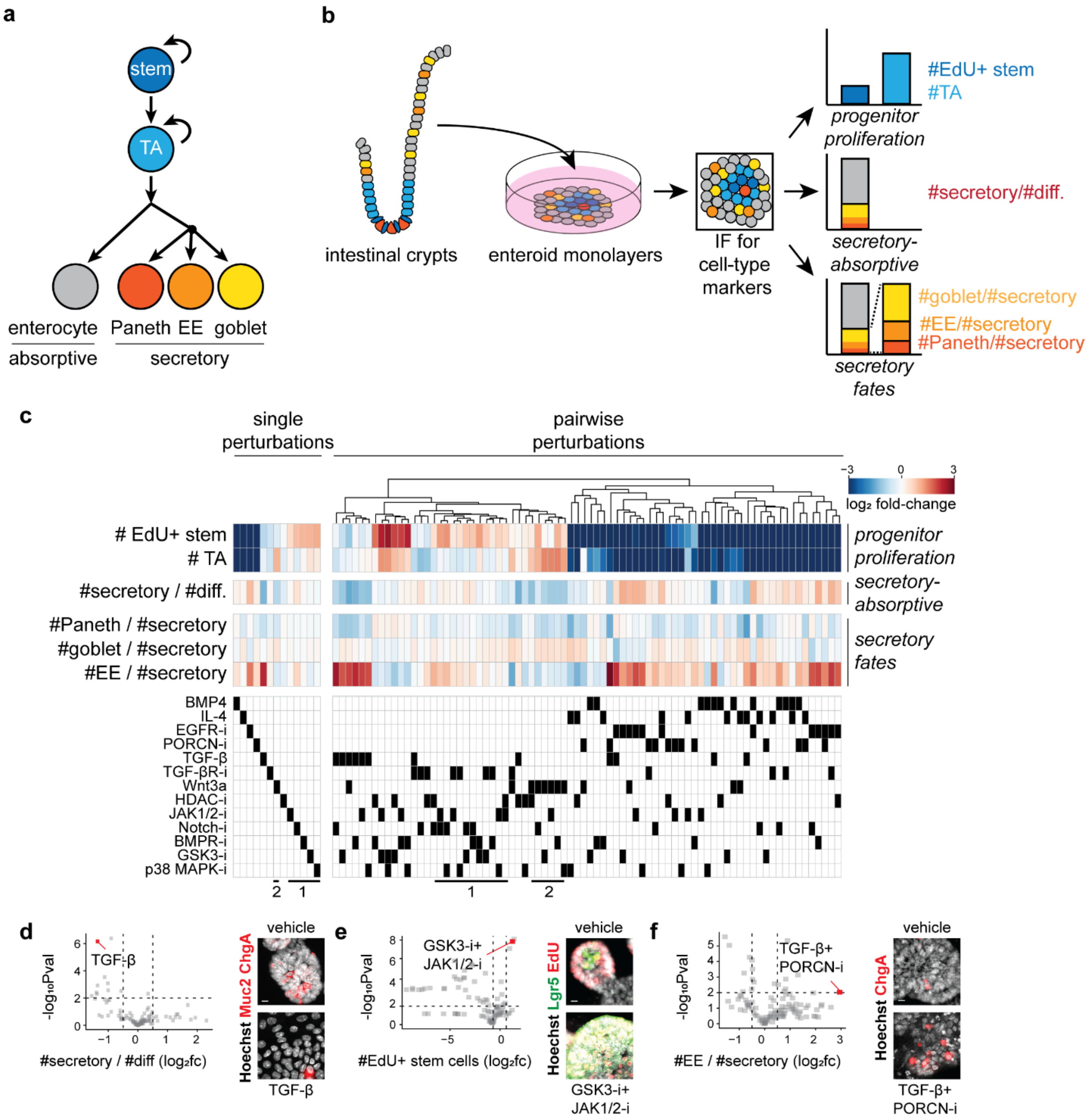

Fig. 1. Systematic characterization of perturbation effects on intestinal epithelial cell-type composition reveals cell-type-specific regulators. a, Intestinal epithelial cell lineage diagram. **b**, Workflow for characterization of perturbation effects on cell-type composition. Intestinal crypts are cultured as enteroid monolayers. Cell-type numbers are measured from

immunofluorescence (IF) images of enteroid monolayers and then combined to readout progenitor proliferation and cell-fate specification. **c**, Combinatorial perturbations induce diverse phenotypes. Single (top) and pairwise (bottom) perturbation effects are shown. Top colored heatmaps: Perturbation effects are represented as $\log_2$ fold-change (fc) relative to vehicle-treated wells. Bottom black-and-white heatmap: Black boxes indicate perturbations in each column. Single perturbations are sorted by #EdU$^+$ stem cells; combinatorial perturbations are clustered based on similarity of tissue-wide effects. Callouts (1) and (2) referred to in text. **d-f**, Combinatorial perturbation experiment reveals regulators of secretory, stem, and EE cell prevalence. Left: volcano plots depicting the magnitude ($\log_2$fc) and significance ($-\log_{10}$Pval) of perturbation effects. Right: images of 3D organoids treated as indicated. Scale bars 5μm. Diff.: differentiated, EE: enteroendocrine.

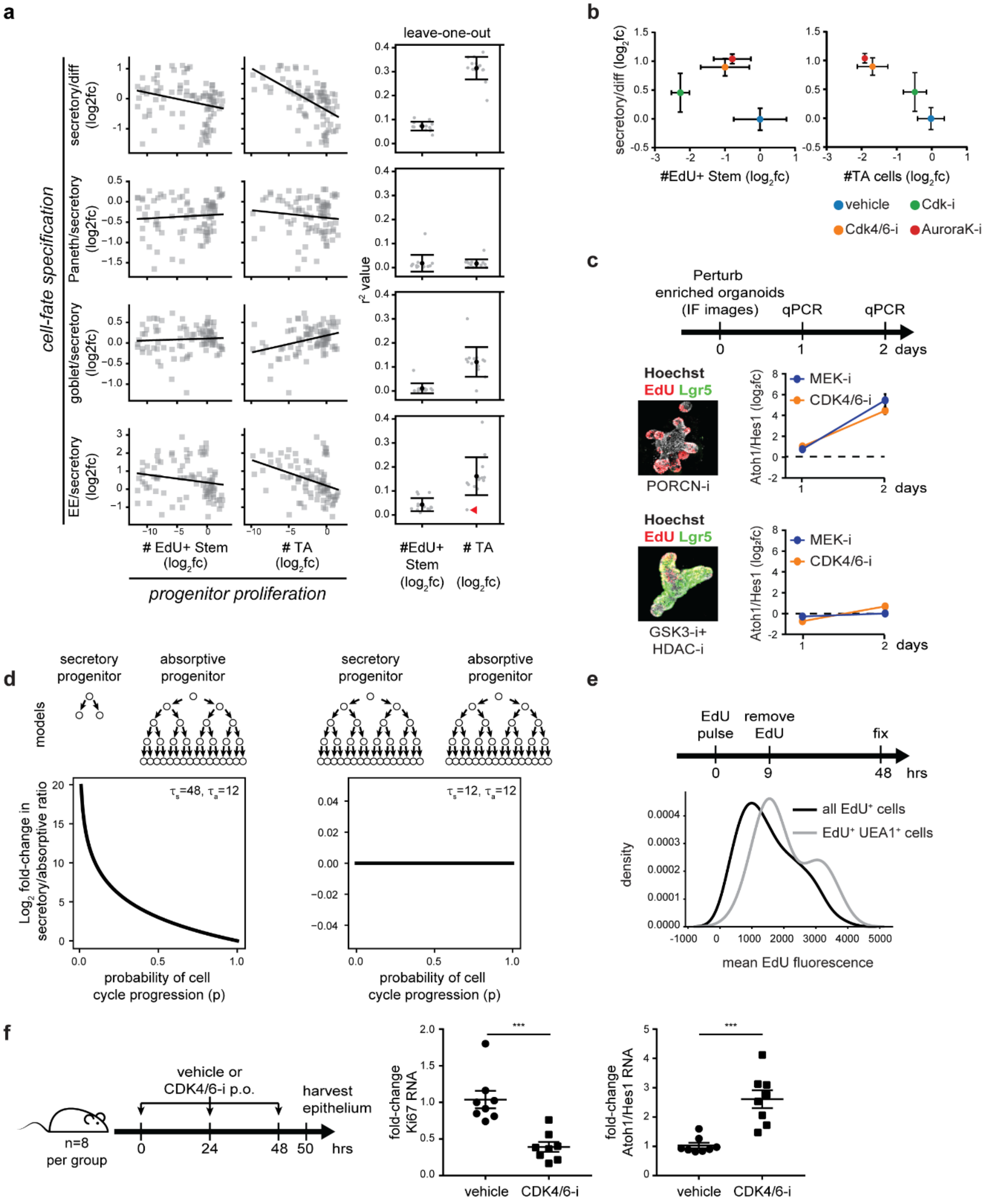

Fig. 2. Changes in transit-amplifying cell proliferation alter secretory cell-type composition. a, Left: Numbers of transit-amplifying (TA) cells, but not EdU$^+$ stem cells, correlate with secretory and EE cell fractions. Perturbation effects (log$_2$fc) are plotted pairwise for each feature. Right: The TA-secretory correlation is not driven by a specific perturbation.

Each of 13 perturbations was sequentially dropped from the dataset and r-squared value calculated. Red arrowhead indicates loss of correlation after dropping EGFR-i. **b**, Inhibiting cell cycle progression increases secretory cell fractions. Enteroids were treated as indicated for 48hrs, after which #EdU$^+$ stem, #TA cells, and #secretory/#differentiated cells were quantified. **c**, TA cells, but not stem cells, are sufficient to alter secretory fractions in response to cell cycle inhibitors. 3D organoids were perturbed into stem or TA cell-rich states using PORCN-i (TA) or GSK3-i+HDAC-i (stem) and then MEK and CDK4/6 inhibitors were applied. The secretory:absorptive ratio was measured at 1 and 2 days post-treatment by qPCR for the ratio of Atoh1:Hes1. **d**, If secretory progenitors divide fewer times than absorptive progenitors, inhibiting the cell cycle increases the secretory:absorptive ratio. Exponential growth model parameters are shown where secretory cell progenitors divide once (τ_s=48hr) and absorptive cell progenitors divide four times (τ_a=12hr) over a 48hr model time (left) compared to where secretory and absorptive cell progenitors both divide four times (τ_s=τ_a=12hr) over a 48-hour model time (right). For other model parameterizations see Supplementary Fig. 7. **e**, UEA1+ secretory cells divide fewer times than other epithelial cells. EdU added for 8hrs to label proliferating progenitor cells and then removed for 48hrs. Enteroids were stained with fluorescent UEA1 to label Paneth and goblet cells, and mean EdU fluorescence measured in all EdU$^+$ cells and EdU$^+$ UEA1$^+$ cells. **f**, Impairing proliferation increases the secretory:absorptive ratio *in vivo*. Mice were treated with CDK4/6-i (palbociclib) or vehicle every 24hr for 48hrs. At 50hrs, intestinal crypts were harvested and gene expression was measured by qPCR. CDK4/6-i decreases Ki67 expression (p=0.0003) and increases the Atoh1:Hes1 ratio (p=0.00005). Error bars mean +/- sem in **b**, **c**, and **f**, and mean+/-sd in **a**. Diff: differentiated, EE: enteroendocrine, TA: transit-amplifying, sec: secretory.

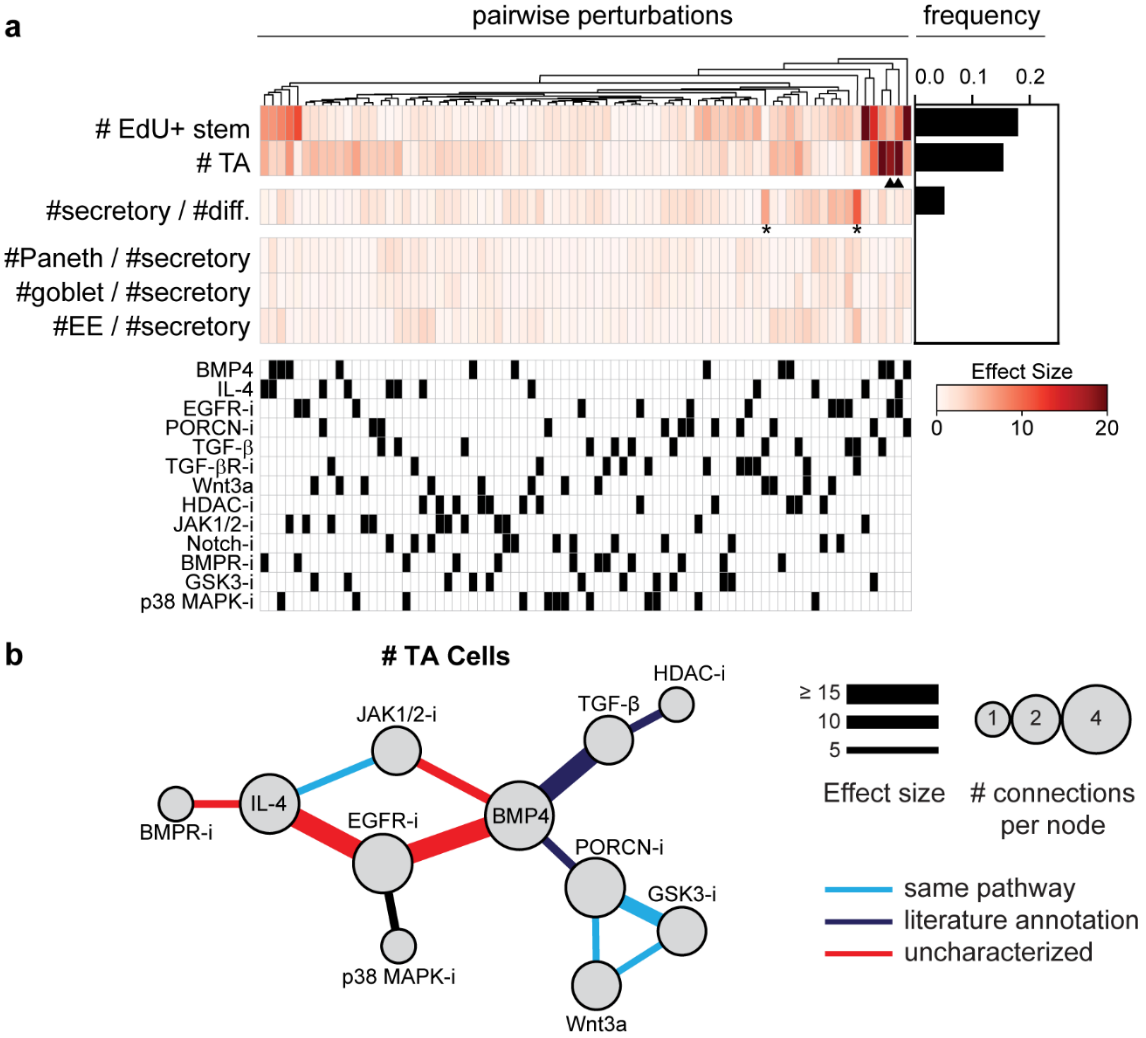

Fig. 3. Interaction mapping reveals cell-type-specific crosstalk controlling transit-amplifying cell proliferation. a, Distinct patterns of signaling crosstalk regulate the abundance of each epithelial cell-type. Left: heatmap of effect size of deviation from predicted multiplicative effect for each perturbation pair across readouts. Stars: TGF-β crosstalk. Arrowheads: TA cell-specific crosstalk involving IL-4, BMP4, and EGFR-i. Right: Frequency of significant deviation (effect size>5) from the multiplicative model predictions for each readout of proliferation and cell-fate specification. **b**, Uncharacterized crosstalk controls transit-amplifying (TA) cell proliferation. Edges represent effect size of deviation from multiplicativity >5. Edge

colors indicate whether perturbations are in the same pathway, previously associated with each other in the intestine or other systems, or uncharacterized.

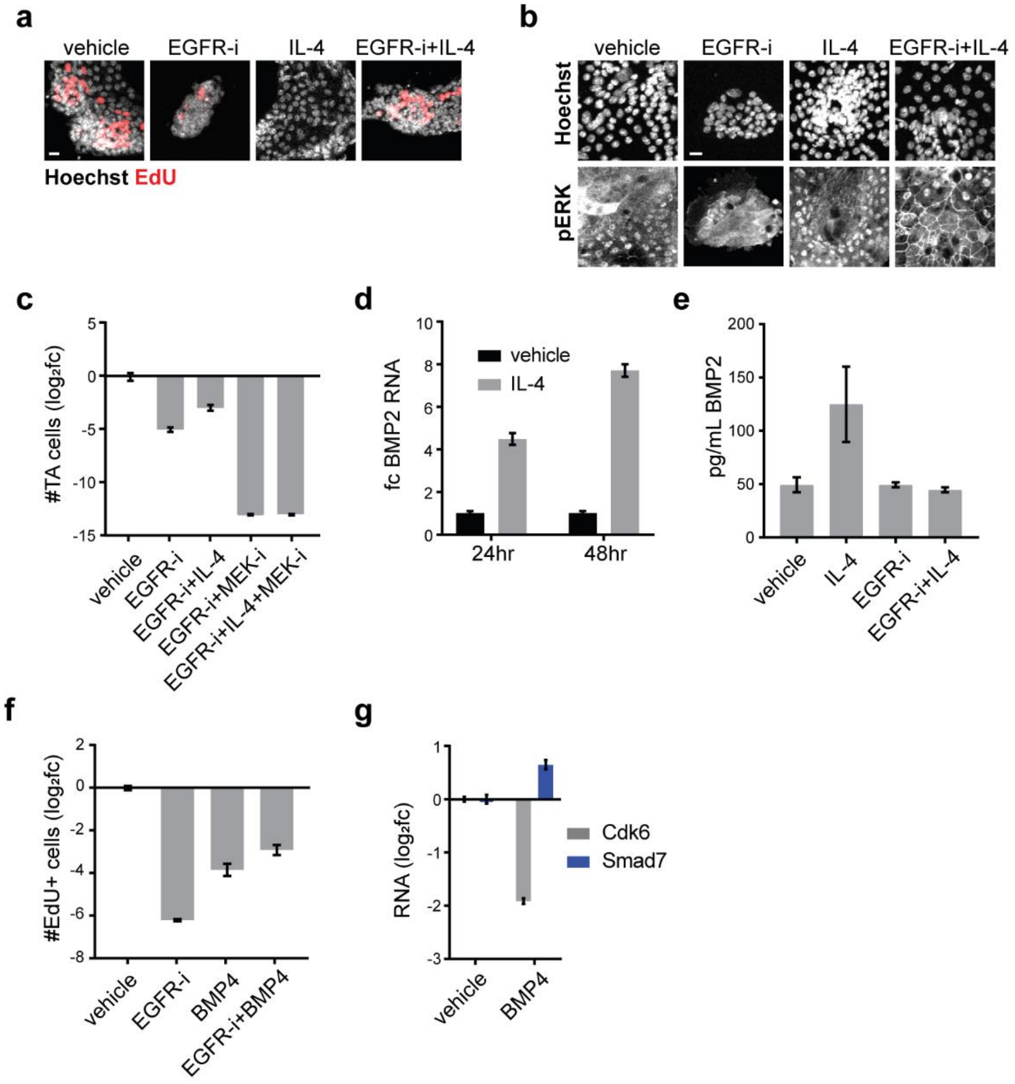

Fig. 4. Transit-amplifying cell-specific crosstalk occurs via convergent regulation of MEK/Erk signaling and paracrine BMP production. a, EGFR-i and IL-4 have mutually antagonistic effects on proliferation. Representative EdU staining images are shown. **b-c**, IL-4 bypasses EGFR inhibition by activating MEK-ERK signaling: **b**, phospho-ERK nuclear translocation is observed in all conditions except EGFR inhibition alone and **c**, mutual antagonism between EGFR-i and IL-4 is dependent on MEK activity. **d**, IL-4 induces BMP2 production. RNA levels of enteroid monolayers were quantified by qPCR. **e**, EGFR-i blocks IL-4-induced BMP2 production. Supernatant levels of BMP2 were measured by ELISA. **f**, The

combination of EGFR-i and BMP4 does not decrease TA cell numbers further than BMP4 alone. **g**, BMP4 reduces Cdk6 expression. RNA levels were quantified by qRT-PCR. Smad7 = known BMP target. Error bars mean+/- sem.

Supplementary Figures

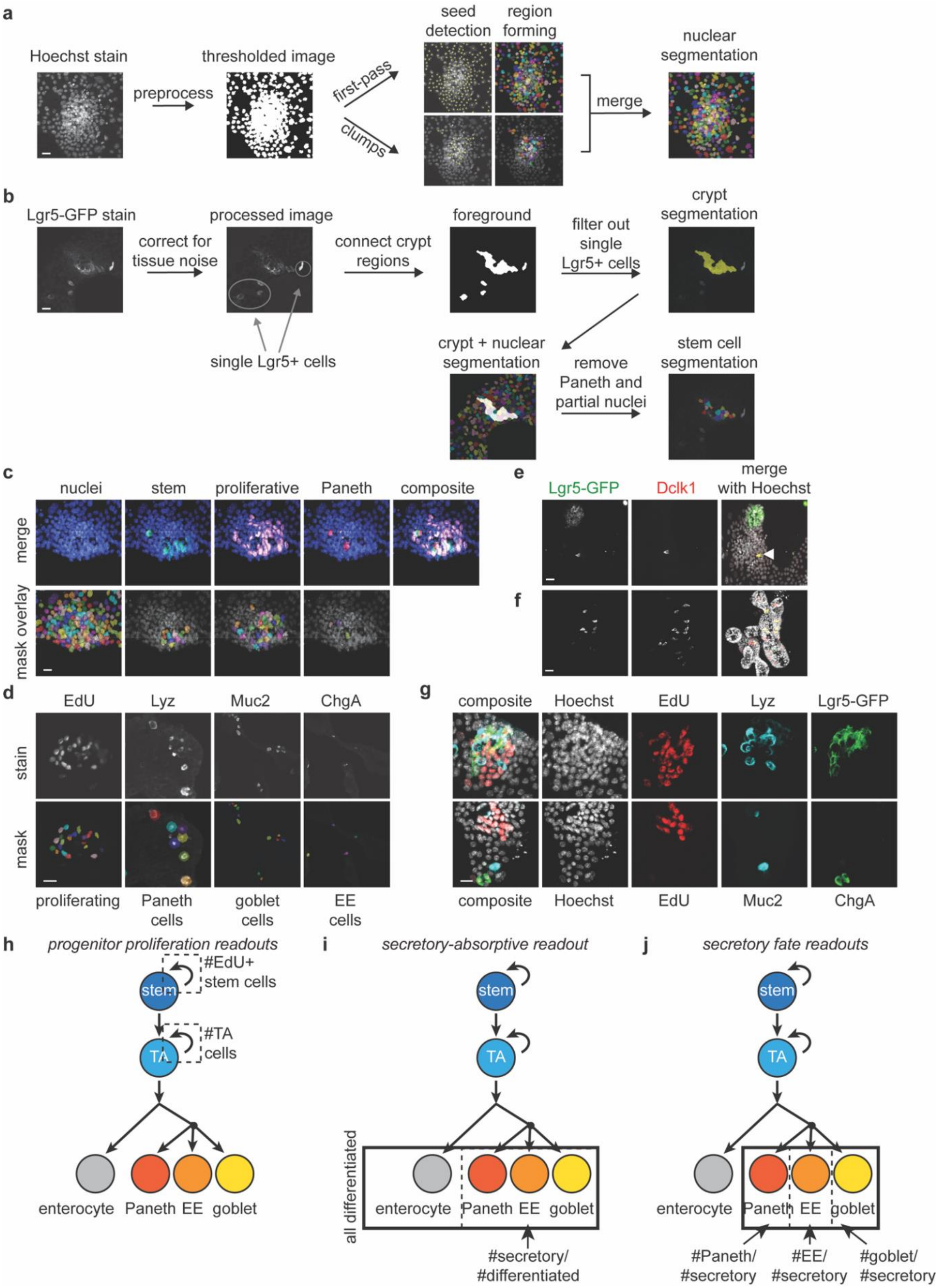

Supplementary Fig. 1. Quantification of progenitor cell proliferation and mature cell-fate

specification in immunofluorescence images of enteroid monolayers. a, Schematic of nuclear segmentation steps. Thresholded Hoechst stain images were segmented in two passes. The first pass segmented sparse nuclei and the second pass segmented clumped nuclei. Sparse and clumped segmentation were merged into the final nuclear segmentation. Yellow dots indicate markers of nuclear objects, multi-pseudocolor overlay depicts individual nuclei segmented from one another using a watershed algorithm. Scale bar 10µm. **b**, Schematic of stem cell segmentation. The Lgr5-GFP stain was first corrected for tissue noise and then thresholded. Size filtering was used to separate multi-cell membrane GFP regions (crypt regions) from single Lgr5-GFP$^+$ cells. All nuclei in crypt regions (nuclei identified from Hoechst image segmentation of same region), with the exception of Paneth cell-associated nuclei, were counted as stem cells. Scale bar 10µm. **c**, Example of crypt segmentation with pseudocolor overlay for each cell-type readout. Scale bar 10µm. **d**, Example of segmentation of proliferating, Paneth, goblet, and enteroendocrine (EE) cells. Top is raw immunofluorescence image for indicated marker and bottom includes pseudocolor overlay of each identified cell object. Scale bar 10µm. **e-f**, Single Lgr5-GFP$^+$ cells are also Dclk1$^+$ in enteroid monolayers (**e**; scale bar 10µm) and 3D organoids (**f**; scale bar 15µm) and are thus excluded from stem cell counts. **g**, Images of two stain sets used in further experiments; stem cell niche-focused stain set which contains Hoechst, EdU, Lyz, and Lgr5-GFP (top; scale bar 7.5µm) and differentiated cell-focused stain set which contains Hoechst, EdU, Muc2, and ChgA (bottom; scale bar 5µm). **h**, Proliferation was quantified as the #EdU$^+$ cells, which was further divided into proliferating stem and transit-amplifying (TA) cells based on Lgr5 staining. **i**, The secretory-absorptive decision was quantified as the % of differentiated cells (EdU$^-$ and Lgr5$^-$) that express secretory markers (the total population of cells that express Paneth (Lyz), goblet (Muc2), or enteroendocrine (EE) cell (ChgA) markers). **j**, Secretory fate bias was quantified as the % of secretory cells that express either goblet, Paneth, or EE cell markers.

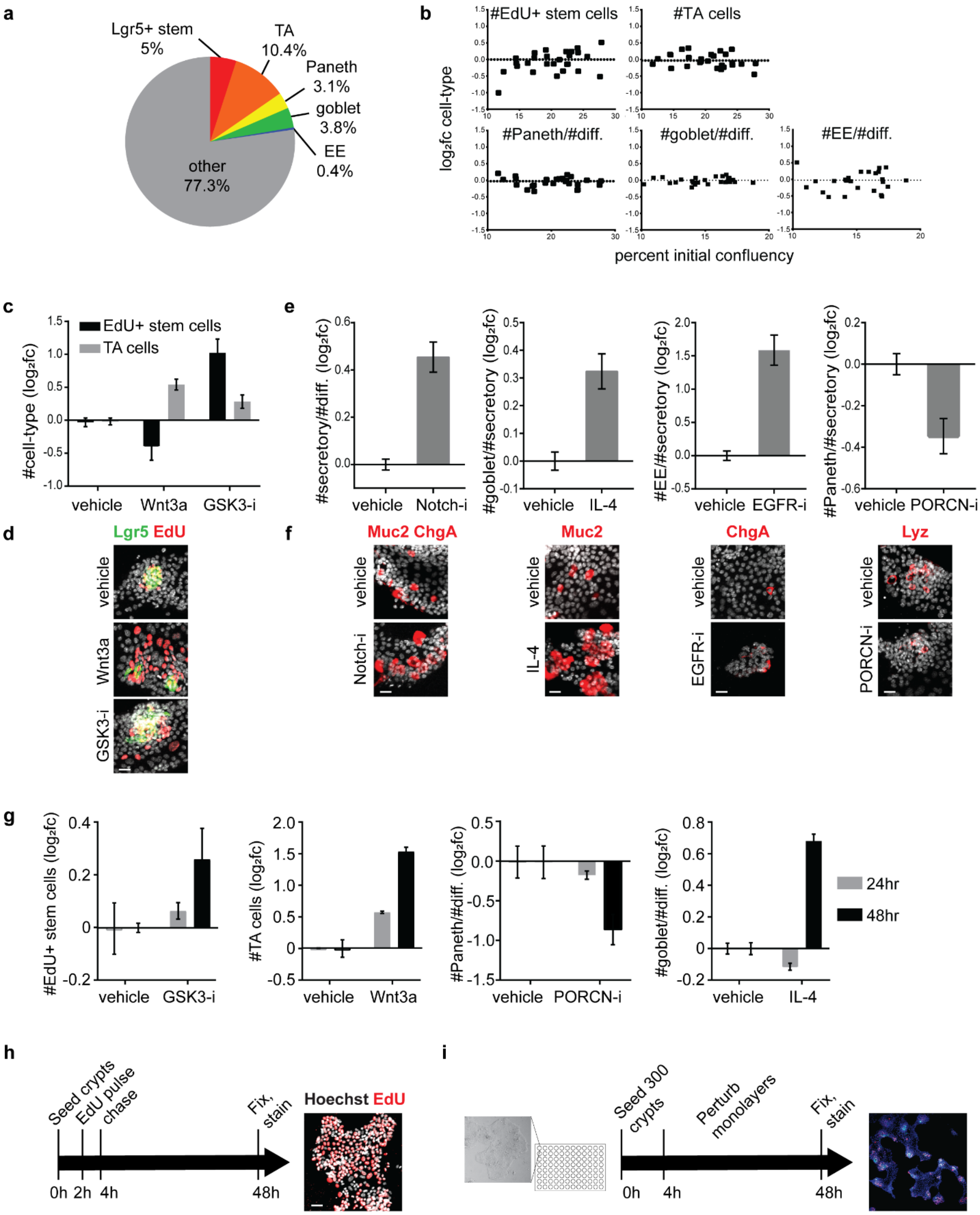

Supplementary Fig. 2. Enteroid monolayers respond reproducibly within 48hrs to known modulators of proliferation and cell-fate specification. a, Combined data from two stain sets in Supplementary Fig. 1g were used to approximate composition of enteroid monolayers, which is similar to *in vivo* reports of small intestinal epithelial cell-type composition (see also Supplementary Table 2). **b**, Enteroid monolayers exhibit reproducible cell-type composition across replicate wells when crypts are seeded at 10-30% initial confluency. Percent initial confluency was measured from brightfield images taken after crypt seeding and 48hr cell-type composition was quantified from immunofluorescence images. Y axis $\log_2$fc was computed relative to average of all wells. No relationship is observed between initial confluency and cell frequencies. **c-f**, Enteroid monolayers respond as expected to modulators of progenitor proliferation (Wnt3a, GSK3-i) and cell-fate specification (Notch-i, IL-4, EGFR-i, PORCN-i). Both quantification of replicate wells (**c, e**) and representative images (**d, f**) are shown. **g**, Enteroid monolayers respond to modulators of TA cell proliferation (Wnt3a) as early as 24hr but do not respond robustly to modulators of stem proliferation (GSK3-i) or cell-fate specification (PORCN-i, IL-4) until 48hr post-perturbation. **h**, The vast majority of cells produced during 48 hours of culture come from initial proliferating progenitor population. Two hours after crypt seeding, EdU was added for 2 hours and then chased for 44 hours. Note that most (~80%) of cells are EdU$^+$. **i**, Schematic of experimental procedure for investigating initial tissue response to perturbation based on time-course and seeding density experiments in panels **b** and **d**. TA: transit-amplifying; diff: differentiated. Error bars mean +/- sem.

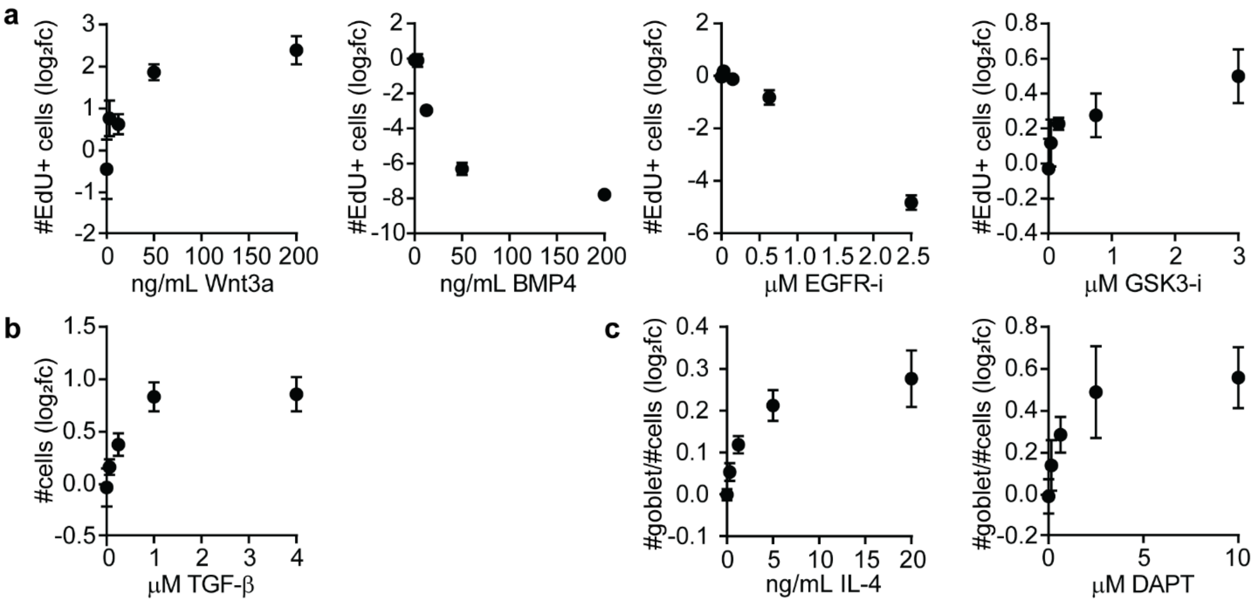

Supplementary Fig. 3. Optimization of perturbation dose. a, Quantification of total proliferating (EdU$^+$) cell numbers after perturbation with increasing doses of Wnt3a, BMP4, EGFR inhibitor, and GSK3 inhibitor. **b**, Quantification of total cell number after perturbation with increasing doses of TGF-β. **c**, Quantification of fraction of goblet cells after perturbation with increasing doses of IL-4 or Notch inhibitor. All data are represented as $\log_2$ transform of the fold-change effect relative to control. Fraction of goblet cells was calculated as a percentage of all cells for comparison with previous studies. Error bars mean +/- sem.

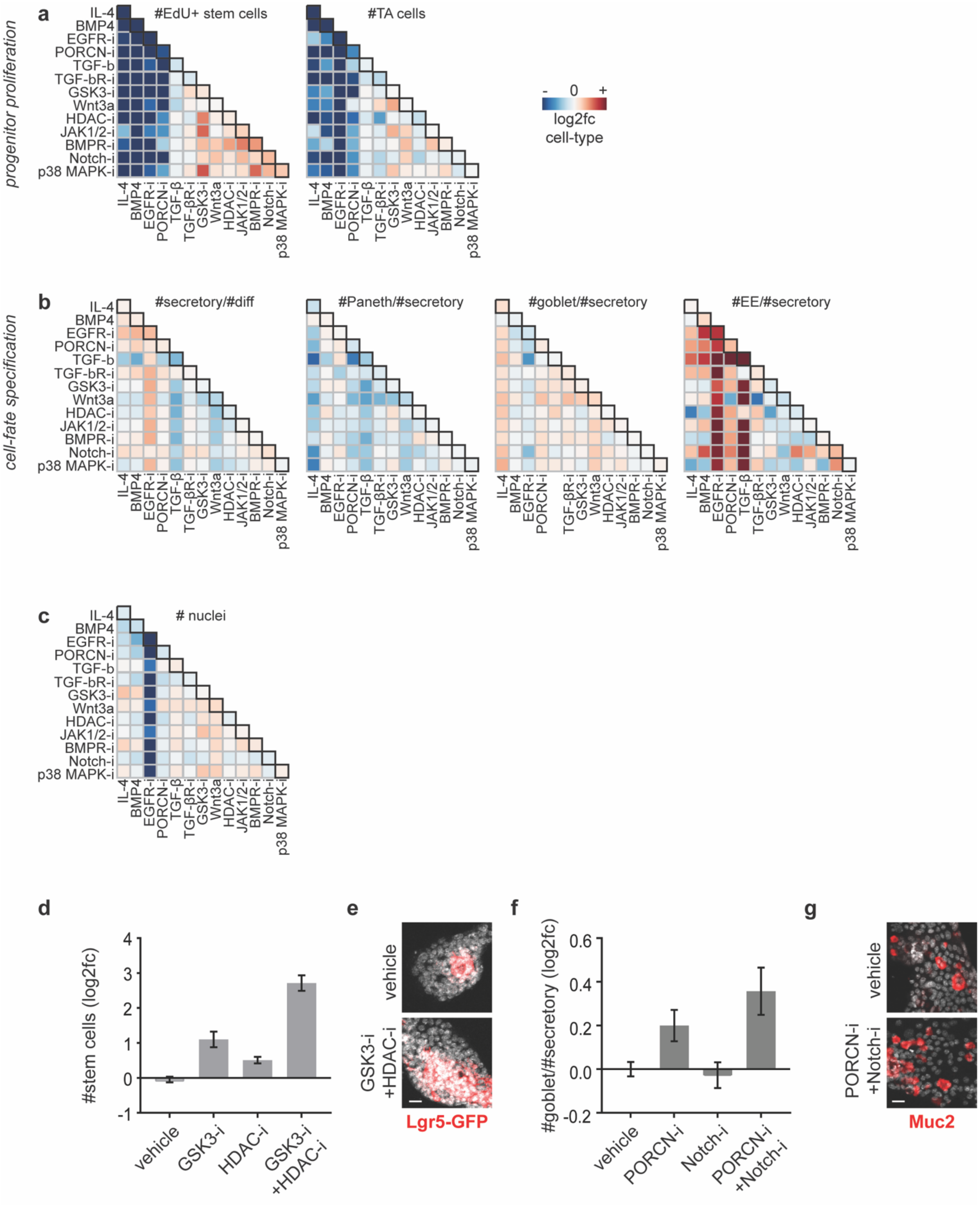
a
progenitor proliferation
#EdU+ stem cells
#TA cells
IL-4
BMP4
EGFR-i
PORCN-i
TGF-b
TGF-bR-i
GSK3-i
Wnt3a
HDAC-i
JAK1/2-i
BMPR-i
Notch-i
p38 MAPK-i
TGF-β
TGF-βR-i
- 0 +
log2fc
cell-type
b
cell-fate specification
#secretory/#diff
#Paneth/#secretory
#goblet/#secretory
#EE/#secretory
c
nuclei
d
#stem cells (log2fc)
4
3
2
1
0
-1
vehicle
GSK3-i
HDAC-i
GSK3-i +HDAC-i
e
vehicle
GSK3-i +HDAC-i
Lgr5-GFP
f
#goblet/#secretory (log2fc)
0.6
0.4
0.2
0.0
-0.2
vehicle
PORCN-i
Notch-i
PORCN-i +Notch-i
g
vehicle
PORCN-i +Notch-i
Muc2

Supplementary Fig. 4. Alternative depiction of single and combinatorial perturbation data as individual cell-type and recapitulation of known combinatorial perturbation effects. a, Quantification of the proliferation readouts; changes in #EdU$^+$ stem cells and #TA cells. **b**, Quantification of cell-fate specification readouts; changes in fraction of differentiated cells positive for secretory cell markers and secretory cells positive for Paneth, goblet, and enteroendocrine (EE) cell markers. **c**, Quantification of the number of nuclei per well. **d**,**e**, Combinatorial perturbations that are known to upregulate stem cells (**d, e**) and goblet cells (**f, g**) exhibit expected effects on enteroid monolayers[7,19]. All perturbations were applied for 48hrs. Quantification of effects on replicate wells (**d, f**) and images (**e, g**) are shown. Scale bars 10µm. Error bars mean +/- sem.

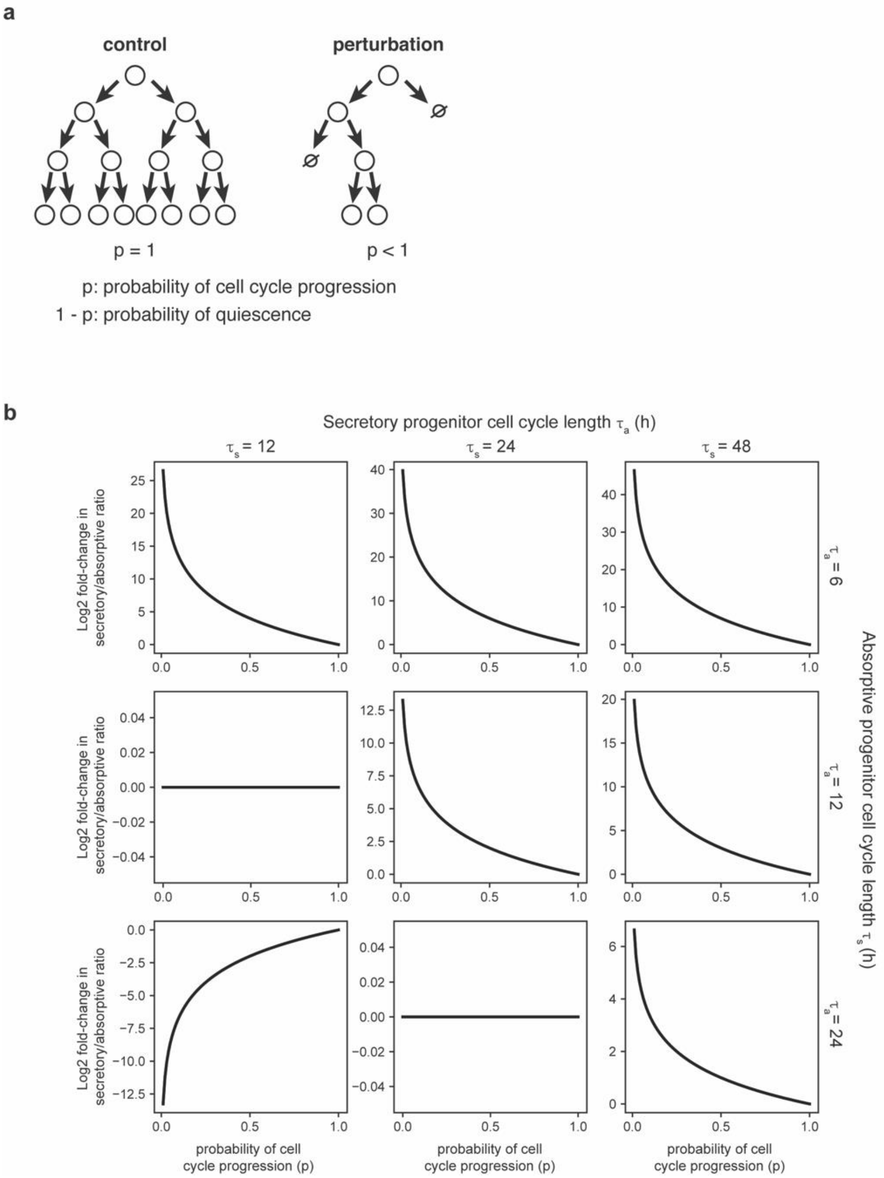

Supplementary Fig. 5. Cell cycle modulators affect the secretory:absorptive ratio due to differential amplification of secretory and absorptive progenitors. a, Diagram of the effect of altering p, a parameter setting the probability of progenitor cell cycle progression. **b**, Exponential growth model supports the hypothesis that secretory progenitors divide fewer times than absorptive progenitors. The parameters τ_a and τ_s describe how often secretory and absorptive progenitors divide. Only when secretory progenitors undergo fewer divisions than absorptive progenitors during the 48 hour simulation period ($\tau_s > \tau_a$) does decreasing the probability of cell cycle progression increase the secretory:absorptive ratio, and vice versa.

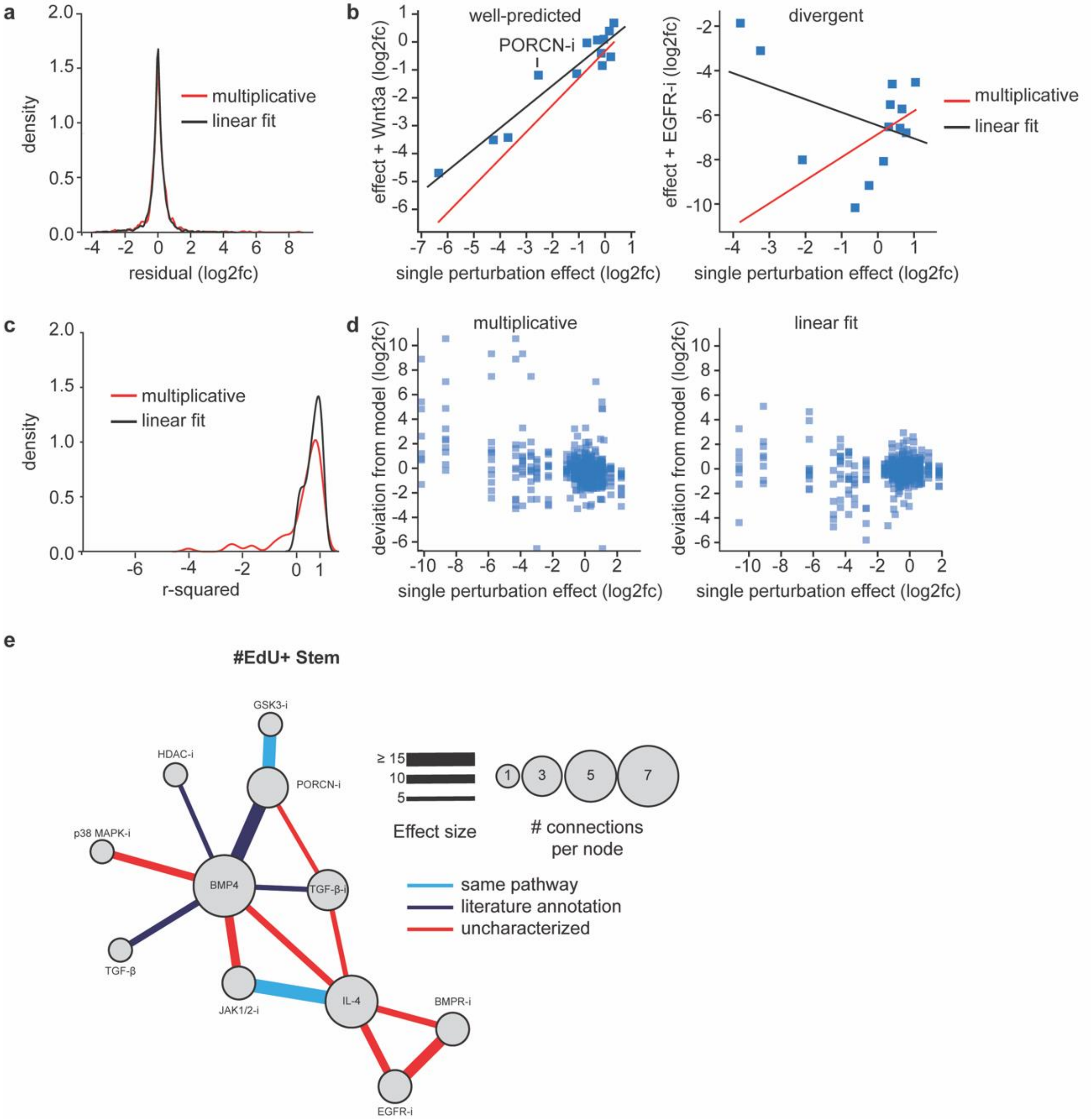

Supplementary Fig. 6. Evaluation and application of linear-fit and multiplicative models. a, Perturbation effects are generally predicted by linear-fit and multiplicative models. Distribution of residual between predicted and observed values across all cell-type readouts is shown for the multiplicative model (red) and linear-fit model (black). **b**, Individual perturbations are either predicted by linear-fit and multiplicative models or diverge significantly from both. Examples of well-predicted (Wnt3a) and divergent (EGFR-i) perturbations are shown. Effects shown are on #TA cells. Both models predict crosstalk between inhibition of PORCN, an enzyme required to process epithelial-intrinsic Wnt3a, and Wnt3a treatment (left). **c**, The multiplicative model fits the data similarly well to a linear model. An r-squared value was calculated for the multiplicative and linear fit models for each perturbation and cell-type (using graphs similar to **b**, see Methods and Supplementary Discussion). The distribution of r-squared values was plotted. **d**, There is no correlation between perturbation effects and double perturbation deviation from multiplicative and linear fit models. For each model, the deviation from model (similar to residual in **a, b**) was plotted against the effect of each single perturbation for all cell-types. **e**, Network diagrams constructed using a force-directed graphing layout algorithm for perturbation pairs whose combinatorial effect deviates from the multiplicative model expectation for the #EdU$^+$ stem cells. Edge colors indicate perturbations are in the same pathway, previously associated with each other in the intestine or other systems, or uncharacterized. Edge width indicates effect size of deviation from multiplicativity >5.

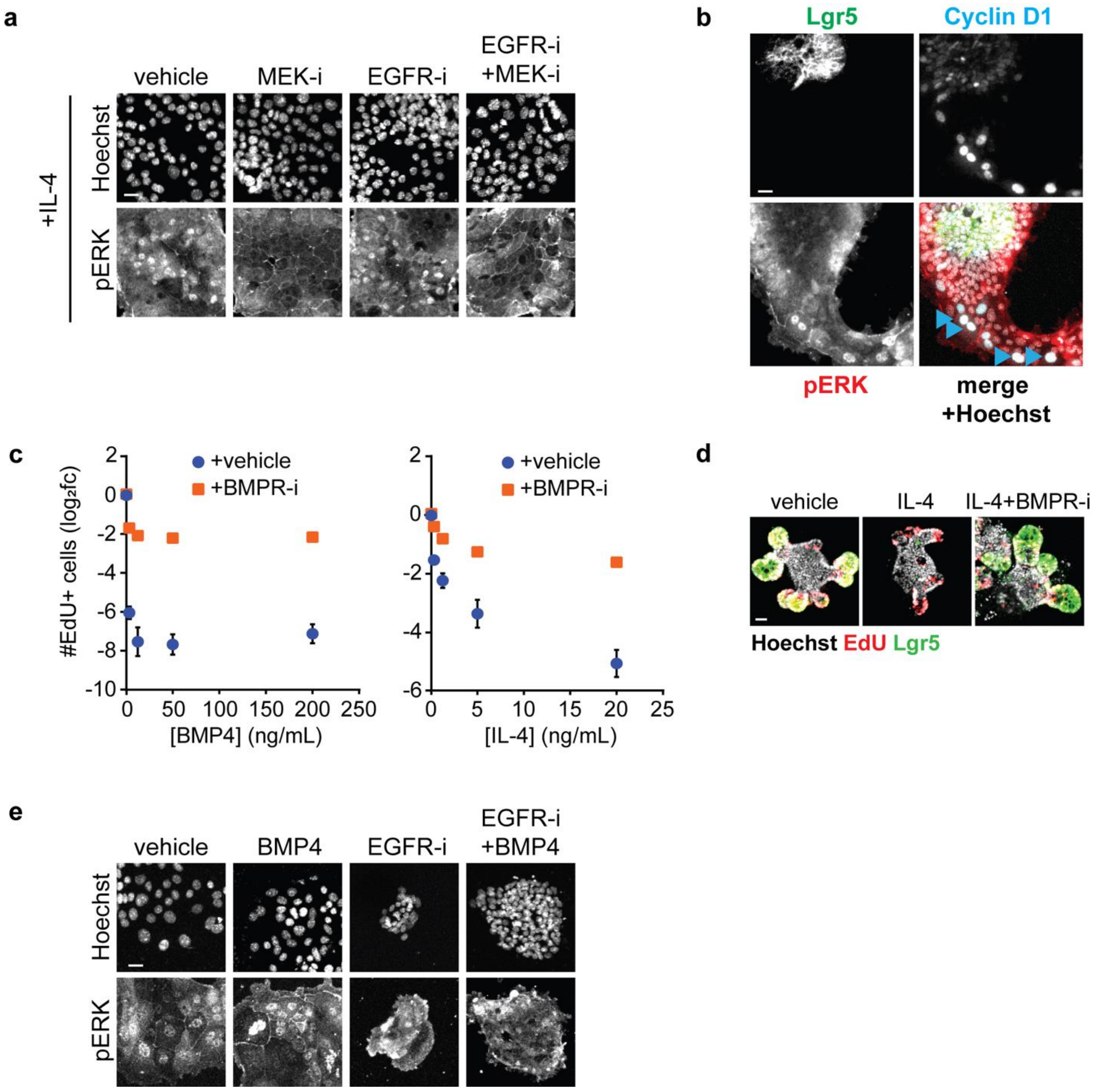

Supplementary Fig. 7. Crosstalk between IL-4, BMP4, and EGFR-i is due to regulation of BMP production and activation of MEK/Erk signaling. a, MEK inhibition reduces Erk activation (nuclear translocation of phospho-Erk) in enteroid monolayers. Enteroid monolayers were treated with the indicated compounds for 24hr and then stained for phospho-Erk1/2. Scale bar 7.5μm. **b**, phospho-Erk nuclear translocation is observed in Cyclin D1^{+} cells but not Lgr5^{+}

cells. Arrowheads indicate cells with nuclear phospho-Erk and Cyclin D1 staining. Scale bar 7.5µm. **c**, BMP receptor inhibition blocks BMP4- and IL-4-induced downregulation of proliferation to similar extents over a range of doses. Enteroid monolayers were treated with increasing concentrations of BMP4 or IL-4 in the presence or absence of BMP receptor inhibitor (BMPR-i) for 48hrs and #EdU$^+$ cells per well were quantified. **d**, BMP receptor inhibition blocks IL-4-induced downregulation of proliferation and stemness in 3D organoids. 3D organoids were treated with vehicle or IL-4 in the presence and absence of BMP receptor inhibitor for 48hrs and then stained for proliferating cells (EdU$^+$) and stem cells (Lgr5$^+$). Scale bar 20µm. **e**, BMP4 does not alter MEK/Erk signaling under vehicle or EGFR-i treatment. Staining from 48hrs of treatment with the indicated compounds is shown. MEK/Erk phosphorylation and nuclear translocation is observed upon vehicle or BMP4 treatment but not under EGFR-i or EGFR-i+BMP4 treatment. Error bars mean +/- sem. Scale bar 10µm.

Supplementary Tables

Cell-type	**Marker**	**Precision**	**Recall**	**F1 Score**
nuclei	Hoechst	0.9965	0.9936	0.9951
goblet cells	Muc2	1	0.8998	0.9473
EE cells	ChgA	0.8551	0.9248	0.8886
Paneth cells	Lyz	0.9018	0.9642	0.9319
EdU$^+$ cells	EdU	1	0.9557	0.9774
crypt regions	Lgr5-GFP	0.9816	0.9877	0.9846
stem cells	Lgr5-GFP	0.9724	0.9756	0.9740
Lgr5$^+$/Dclk1$^+$ cells	Lgr5-GFP	0.8208	0.9087	0.8625

Supplementary Table 1. Evaluation of the performance of cell-type identification algorithms.

Cell Type	***In Vivo* (%)**	**2D (%)**
Enterocyte	80[13]	77.3
Paneth	7.5% of crypt cells[30]	3.1% of all cells
Goblet	4-6[30]	3.8
EE	0.6[30]	0.4

Supplementary Table 2. Comparison of enteroid monolayer cell-type composition with literature reports of small intestine cell-type composition.

Pathway	**Perturbation**	**Target**	**Designation**	**Effect on Pathway**	**Published Effect(s) on Intestinal Epithelium**	**Dose Ref.**
EGFR	erlotinib	EGFR	EGFR-i	inhibit	Reduced proliferation, increased EE cell specification[8]	8
Wnt	Wnt3a	Frizzled	Wnt3a	activate	Increased proliferation[31]	4
	IWP-2	PORCN	PORCN-i	inhibit	Decreased proliferation, stem cells, Paneth cells [8,9,15,32]	6
	CHIR99021	GSK3	GSK3-i	activate	Increased proliferation, stem cells[6]	6
BMP	BMP4	BMPR	BMP4	activate	Decreased proliferation and stem cells[10]	4
	LDN-193189	ALK2/3	BMPR-i	inhibit	Increased proliferation and stem cells[33]	4
TGF-β	TGF-β	TGF-βR	TGF-β	activate	Important for differentiation *in vivo*[33–35]	36
	EW-7197	ALK4/5	TGF-βR-i	inhibit	?	37
Notch	DAPT	γ-secretase	Notch-i	inhibit	Increased secretory cell-types[38]	6
IL-4-JAK	IL-4	IL-4R	IL-4	activate	Increased goblet cells[7]	7
	baricitinib	JAK1/2	JAK1/2-i	inhibit	Altered stem cell numbers[11,12]	39
HDAC	valproic acid	HDAC1/2	HDAC-i	inhibit	Increased stem cells[6,7]	6
p38 MAPK	SB202190	p38 MAPK	p38 MAPK-i	inhibit	Increased proliferation[40,41]	41

Supplementary Table 3. Selection of cell-fate perturbations for study. For each perturbation, the specific pathway and target are indicated, as is the expected effect on the pathway and tissue. Designation is the code with which the perturbation is referred to in figures and text.

Supplementary Methods

Mice

All animal care and experimentation was conducted under protocol AN-179937 agreed upon by the Administrative Panel on Laboratory Animal Care at the University of California, San Francisco. All our animal studies are performed in full accordance with UCSF Institutional Animal Care and Use Committee (IACUC). 5- to 6-week-old male C57BL/6 mice (C57BL/6NHsd) were purchased from Harlan and housed with ad libitum food and water on a 12hr light cycle at the UCSF Preclinical Therapeutics Core vivarium.

Media

Organoid basal media (OBM) consists of Advanced DMEM/F12 with non-essential amino acids and sodium pyruvate (Fisher Scientific #12634-028) containing 1x N-2 (Fisher Scientific #17502-048), 1x B-27 (Invitrogen #17504-044), 10 mM HEPES (Invitrogen #15630080), 1x GlutaMAX (Invitrogen #35050-061), 1 µM N-acetylcysteine (Sigma Aldrich #A9165), 100 U/mL penicillin and 100 µg/mL streptomycin (Corning #30-002).

For initial seeding, enteroid monolayers were maintained in OBM supplemented with 3 µM CHIR-99021 (Sigma Aldrich #SML1046), 50 ng/mL murine EGF (Invitrogen #PMG8043), 1 µM LDN-193189 (Sigma Aldrich #SML0559), 500 ng/mL murine R-spondin-1 (Peprotech #315-32), and 10 µM Y-27632 (Selleck Chemicals #S1049).

4 hours after initial seeding, media was changed into OBM supplemented with 50 ng/mL murine EGF, 100 ng/mL murine Noggin, and 500 ng/mL murine R-spondin-1. Perturbations applied in the studies described here were all applied in the background of this medium.

Enteroid monolayer cultures

Enteroid monolayers were derived as previously described[4]. Briefly, jejunum was isolated from male mice between 6-12 weeks of age. Mice used were either from the C57BL/6 strain or, when indicated, the Lgr5$^{eGFP\text{-}DTR}$ strain[42] (kind gift of Frederic de Sauvage, Genentech via Ophir Klein under MTA #OM-216813). Epithelium was released from jejunal tissue by incubation in ice-cold PBS with 3 mM EDTA in PBS (Ambion #9260). Released epithelial tissue was washed 3x with OBM, after which crypts were separated from villus material using 100 and 70 µm cell strainers (BD Falcon) in succession. Crypts were resuspended in seeding media and plated on Matrigel (Thermo Fisher #CB-40234C)-coated 96-well optical bottom plates (BD Biosciences #353219 and Greiner #655090). Typically, 300 crypts were seeded per well. We identified this seeding density because, at this density, we did not observe an effect of variations in initial confluency on cell outgrowth (#cells) or cell-type composition (Supplementary Fig. 2b). Four hours after seeding, cells were washed with OBM and incubated in control media containing other perturbations of interest.

3D organoid cultures

3D organoids were cultured as previously described[43]. For imaging experiments, 3D organoids were seeded in 10 µL of Matrigel in 96-well optical bottom plates.

CDK4/6-i administration to mice and tissue harvest

To test the effects of cell cycle inhibition on the secretory:absorptive ratio, palbociclib (LC Laboratories #P-7744) at 150 mg/kg in 50 mM sodium lactate buffer pH 4.4 was administered to mice by oral gavage every 24 hours for 48 hours (at 0 hours, 24 hours, and 48 hours). At 50 hours, the small intestine was harvested and intestinal crypts were harvested as described in the enteroid monolayer culture' section above. Crypts were lysed in Buffer RLT (RNEasy Kit, Qiagen) for subsequent RNA purification.

Growth factors and chemical compounds

All growth factors and chemical compounds were purchased from suppliers and used as designated without further purification. Unless otherwise indicated, perturbations were used as follows:

Perturbation	**Vendor and Catalog #**	**Concentration**
DAPT (Notch-i)	Stemgent #04-0041	10 µM
CHIR-99021 (GSK3-i)	Sigma Aldrich #1046	3 µM
Valproic acid (HDAC-i)	Sigma Aldrich #P4543	1 mM
IWP-2 (PORCN-i)	Selleck Chemicals #S7085	2 µM
Wnt3a	R&D Systems #5036-WN-500	200 ng/mL
TGF-β	PeproTech #100-21C	4 ng/mL
EW-7197 (TGF-βR-i)	Selleck Chemicals #S7530	1 µM

BMP4	R&D Systems #314-BP-010	200 ng/mL
LDN-193189 (BMPR-i)	Sigma Aldrich #SML0559	1 μM
Baricitinib (JAK1/2-i)	Selleck Chemicals #S2851	2 μM
SB202190 (p38MAPK-i)	Sigma Aldrich #S7067	10 μM
IL-4	PeproTech #214-14	20 ng/mL
Erlotinib HCl (EGFR-i)	Selleck Chemicals #S1023	2.5 μM
PD0325901 (MEK-i)	Selleck Chemicals #S1036	1 μM
Palbociclib (PD-0332991) (CDK4/6-i)	Selleck Chemicals #S1116 (organoid studies) or LC Laboratories #-7744 (*in vivo* studies)	10 μM
Flavopiridol (CDK-i)	Selleck Chemicals #S2679	0.3 μM
AT9283 (AuroraK-i)	Selleck Chemicals #S1134	1 μM

Immunofluorescence assay

Enteroid monolayers: Enteroid monolayers were washed 1x with warm D-PBS and then fixed with 4% paraformaldehyde in PBS for 15min at room temperature. Cells were then washed with PBS and permeabilized with 0.5% Triton-X-100 in PBS at room temperature for 10min. Cells were washed, blocked with 3% BSA in PBS for 30min, and then incubated in primary antibody in antibody buffer (PBS with 0.3% Triton-X-100, 1% BSA) overnight at 4C. The next day, cells were washed and incubated with secondary antibodies and Hoechst 33342 (5 μg/mL; Invitrogen #H3570) in antibody buffer for 2 hours at room temperature. After this, cells were washed with PBS and imaged in TBS-T (0.1% Tween in 1x TBS pH 7.4).

3D organoids: Media was carefully aspirated from around Matrigel domes containing 3D organoids using a P100 pipet. 4% paraformaldehyde in PBS was immediately added for 15min at room temperature. Cells were then washed 2x with PBS and permeabilized using 0.5% Triton-X-

100 in PBS for 20min at room temperature. Cells were then rinsed 3x10min with 100 mM glycine in PBS with gentle agitation. Cells were blocked in 3% BSA in PBS for 40min and then incubated with primary antibody in antibody buffer overnight at room temperature. The next day, cells were washed 3x20min in antibody buffer and then incubated with fluorescent secondary antibodies and Hoechst in antibody solution for 1hr at room temperature. Cells were then rinsed in PBS and stored and imaged in TBS-T.

Antibodies

All antibodies were purchased from suppliers and used as designated without further purification. Unless otherwise indicated, antibodies were used as follows:

Epitope	**Vendor and Catalog #**	**Dilution**
Lysozyme (Lyz)	Dako	1:2000
Mucin-2 (Muc2)	Santa Cruz Biotechnology #15334	1:100
Chromogranin A (ChgA)	Santa Cruz Biotechnology #393941	1:100
GFP	Abcam #5450	1:2000
Dclk1	Abcam #31704	1:1000
Erk1 (pT202/pY204) + Erk2 (pT185/pY187) (pErk)	Abcam #50011	1:200
Phospho-Smad1 (Ser463/465) / Smad5 (Ser463/465) / Smad9 (Ser465/467) (pSMAD1/5/9)	Cell Signaling Technology #13820	1:800
Cyclin D1	Life Technologies #MA5-14512	1:200

EdU pulse and visualization

To visualize proliferating cells (specifically, those in S phase), enteroid monolayers were incubated with 10 µM EdU (Thermo Fisher #A10044) in media (containing indicated perturbations or vehicle) for 2 hrs prior to fixation. After immunofluorescence staining, EdU$^+$

cells were visualized using Click chemistry as previously described[44]. Briefly, cells were incubated with a reaction mixture containing 1 mM CuSO4 (VWR International #470300-880), 5 µM sulfo-Cyanine5 azide (Lumiprobe #B3330) or 5 µM BDP-FL azide (Lumiprobe #11430), and 100 mM sodium ascorbate (Sigma Aldrich #A4034) in PBS for 30min at room temperature.

UEA-1 staining

Fluorescein-conjugated UEA1 (Vector Laboratories #FL-1061) was applied at 1:400 for 30min in TBS-T to label goblet and Paneth cells.

Automated brightfield microscopy

Upon initial plating, enteroid monolayers were imaged in the brightfield channel using the 10x objective of a Nikon TE200-E epifluorescence microscope. These data were used as a control to determine whether enteroid monolayers were seeded at an optimal and consistent confluency.

Quantifying % confluency

% Confluency (percent of image which is occupied by enteroid monolayer cultures) was quantified from brightfield images using a previously reported algorithm (CellularRegionsFromBrightField function in Supplementary Software 1 from reference[45]).

Automated confocal microscopy

Enteroid monolayers were imaged on the 10x objective of a Nikon A1 confocal with Ti2-E microscope. The area of each well was covered by 24 individual scans. In each field of view, 4-8 z planes were collected at 1024x1024 resolution. Importantly, the nuclear stain was used to autofocus in each new field of view.

Immunofluorescence image segmentation and analysis

General information: Image segmentation was performed using a custom Python analysis pipeline. All code and documentation can be found on GitHub. Starting with maximum intensity projections of Hoechst, EdU, Lgr5-GFP, Muc2, Lyz, and ChgA fluorescent images, we segmented and then quantified numbers of nuclei, EdU$^+$ cells, stem cells, goblet cells, Paneth cells, and enteroendocrine cells, respectively. The general segmentation process for each object type consisted of two major steps: a thresholding step to identify image foreground, and a segmentation step to generate location and boundary of objects. Specific details are as follows:

Segmenting nuclei: Hoechst stain images were smoothed through convolution with a bilateral filter. The foreground was identified using a modified Otsu threshold method. Nuclei in enteroid cultures are highly heterogeneous with small, tightly packed nuclei in the crypt regions and large, sparsely distributed nuclei in the villus regions. Therefore, to obtain an accurate segmentation in these different regions, we conducted a two-step segmentation approach. First, sparse nuclei were identified using a multi-scale Laplacian of Gaussian (LoG) detector to generate markers of object locations. A watershed algorithm was then used to generate object boundaries. Clumps were detected in the sparse segmentation using object size and shape irregularity cutoffs. These clumps contained mis-segmented dense nuclei and were subsequently segmented using differently parameterized LoG detector to identify object seeds and watershed to generate object boundaries. The dense and sparse segmentations were then merged for the final result (also see Supplementary Fig. 1a).

Segmenting EdU$^+$ nuclei: The same process as nuclear segmentation was used because nuclear objects in EdU stain images had similar properties as those in Hoechst stain images.

Segmenting stem cells: GFP immunofluorescence in enteroid monolayers derived from Lgr5-eGFP-DTR mice[42] revealed both crypt regions, with multi-cell membrane GFP staining, and single GFP$^+$ cells outside crypt regions. The single GFP$^+$ cells appeared morphologically similar to tuft cells and co-stained for Dclk-1 (Supplementary Fig. 1e-f), indicating that these cells are likely a subpopulation of tuft cells rather than stem cells. Therefore, we only identified stem cells within crypt regions. Crypt regions were defined as clusters of Lgr5$^+$ stem and Paneth cells, corresponding to crypt bases *in vivo*. Lgr5-GFP stain images were processed to remove tissue background and thresholded to identify foreground. Holes and gaps in crypt regions were filled using morphological operations and small objects (typically, Lgr5$^+$/Dclk1$^+$ cells, see Supplementary Fig. 1e-f) were dropped. The remaining objects were labeled as crypts. We then counted nuclei within crypt regions as stem cells. Importantly, we removed any nucleus in a crypt region that was associated with a Paneth cell from the stem cell count.

Identifying Paneth cells: Lysozyme (Lyz) immunofluorescence images were smoothed through convolution with a bilateral filter then a tophat filter. Foreground was identified using the Otsu-thresholded Lyz immunofluorescence image. A LoG detector was then used to generate markers of Paneth object locations.

Segmenting goblet cells: Mucin-2 (Muc2) stain images were smoothed by convolution with a median filter. Foreground was identified using a convex hull of objects in each Otsu-thresholded Muc2 immunofluorescence image. Goblet cells were segmented using a LoG detector to generate markers of goblet object locations followed by watershed to create object boundaries.

Identifying enteroendocrine (EE) cells: ChgA stain images were processed using the same steps as Paneth cell identification, only with different parameters.

Evaluation of Image Segmentation: Each cell-type object (e.g., each nucleus, each goblet cell, each Paneth cell) was identified in raw immunofluorescence images by hand by an expert and, in parallel, using the customized algorithms described above. The expert-generated segmented images (where each mask represents an individual object) were compared to algorithm-generated segmented images to determine algorithm performance. 'Precision' was quantified by dividing the number of true positives (expert-identified objects also identified by the algorithm) by the number of total positives (all algorithm-identified objects). 'Recall' was quantified by dividing the number of true positives by the total number of expert-identified objects. F1 scores were calculated as the harmonic mean of precision and recall. See Supplementary Table 1 for results.

Data Analysis

Extracting numbers of each cell-type: Due to limitations of conventional fluorescence microscopy, all desired cell-types were quantified across two replicate immunofluorescent stain sets: a crypt stain set (Hoechst, EdU, Lgr5-GFP, Lyz) and a differentiated cell stain set (Hoechst, EdU, Muc2, ChgA). We were able to quantify the numbers of some cell-types directly from a single stain set, including the number of each directly measured cell-type (EdU$^+$, stem, goblet, Paneth, EE) as well the number of proliferating (EdU$^+$) stem cells (combining information from EdU and Lgr5-GFP segmentation), transit-amplifying cells (TA; #EdU$^+$ cells minus #stem cells), and differentiated cells (# cells minus stem and TA cells). By combining information from across both stain sets, we captured the process of cell-fate specification: both the approximate fraction of secretory cells within the differentiated cell population (#goblet + #Paneth + #EE divided by #differentiated; #secretory/#diff) and; the fractions of each secretory cell-type (goblet, Paneth, EE) to the total secretory population (#goblet/#secretory, #Paneth/#secretory, #EE/#secretory). Also see Supplementary Fig. 1h-j and Supplementary Discussion on readouts representing the processes of proliferation and cell-fate specification.

Replicates and Error Estimation: In-plate replicate control wells (2-6 wells per plate) were used to estimate mean and error. For replicate plates, mean and error were pooled. For across stain-set readouts, error was propagated. Errors for features that were not observed was dropped during error propagation.

Fold Change: We calculated fold-change effects relative to in-plate controls for readouts within each stain set (#EdU$^+$ stem cell, #TA cells). Fold-changes for readouts calculated across both stain sets (#secretory/#diff, #goblet/#secretory, #Paneth/#secretory, #EE/#secretory) were calculated to a pooled control baseline measurement.

Perturbation effect visualization

For Fig. 1c and Fig. 3a, double perturbation phenotypes were sorted into similar phenotypes using hierarchical clustering (clustermap function in seaborn) with a euclidean distance metric. Single perturbation phenotypes were sorted based on the number of EdU$^+$ stem cells in each row. For Supplementary Fig. 4a-c, perturbations were sorted by the number of stem cells (EdU$^+$ and EdU$^-$) in each well (stem cell data not shown).

Population growth model

A population growth model was established to capture the changes in secretory and absorptive populations in response to cell cycle perturbation. In this model, we assumed that the initial ratio of absorptive to secretory TA progenitors produced by stem cells is equal. After this, the progenitors are locked into either secretory or absorptive fates and there is no switching between fates[16,46].

Under normal growth (control condition), we describe the amplification of absorptive and secretory TA cells as follows:

$$E(A) = A_0(2)^{\frac{t}{\tau_a}}$$
$$E(S) = S_0(2)^{\frac{t}{\tau_s}}$$

where A_0 and S_0 are the numbers of initial absorptive and secretory TA progenitors, respectively. A and S are the numbers of final absorptive and secretory differentiated cells, respectively. t is the total model time, set to be 48 (hours). τ_a and τ_s are the cell cycle lengths of absorptive and secretory progenitors, respectively. Absorptive progenitors are generally found to divide 4-5 times while secretory progenitors only divide 1-2 times[16,46,47]. Thus, τ_a and τ_s are set to be 12 and 48 (hours) in control conditions. Thus, in this model, secretory progenitors divide once while absorptive progenitors divide four times before fully differentiating.

We model the perturbation effect with the parameter p, where p is the probability of cell cycle progression for any TA cell (alternatively 1 – p is the probability of quiescence). The expected numbers of differentiated absorptive and secretory cells, as averaged over an ensemble, are as follows:

$$E(A) = A_0(2p)^{\frac{t}{\tau a}}$$
$$E(S) = S_0(2p)^{\frac{t}{\tau_s}}$$

where 0 < p < 1 in the case of cell cycle inhibitors and p = 1 in the untreated case.

Scanning through different values of τ_a and τ_s , we observe that as long as τ_a is shorter than τ_s, decreasing proliferation (increasing p) corresponds to an increase in secretory fate bias.

We note that we can take a different parametrization for the cell-cycle inhibitor effect where the length of cell cycling is varied. The equations for this parametrization are as follows:

$$E(A) = A_0(2)^{\frac{t}{p'\tau_a}}$$
$$E(S) = S_0(2)^{\frac{t}{p'\tau_s}}$$

where we take p' to be a number > 1 in the case of cell cycle inhibitors and p = 1 in the untreated case and t is 48 as before. Since we can convert between p' and p by letting $p = 2^{\frac{1}{p'}-1}$, we would observe a similar outcome as the first parametrization where increasing perturbation effect via increased cell cycle inhibition corresponds to increasing bias for the secretory fate.

Identifying perturbation crosstalk

Multiplicative model: In a multiplicative model, the combination effect of adding treatment A and treatment B is the multiplication of the fold-change effects of treatment A and treatment B alone: $\mathrm{fc}(AB_{\mathrm{predicted}}) = \mathrm{fc}(A_{\mathrm{obs}}) * \mathrm{fc}(B_{\mathrm{obs}})$. We $\log_2$ transformed fold-change effects prior to calculating expected effects because $\log_2$ transforms make the comparison of increased and decreased fold-change effects more intuitive. Thus, our multiplicative model was a ‘log-additive’ model: $\log_2\mathrm{fc}(AB_{\mathrm{predicted}}) = \log_2\mathrm{fc}(A_{\mathrm{obs}}) + \log_2\mathrm{fc}(B_{\mathrm{obs}})$. Features with 0 values had a pseudocount of 1 instead. (also see Supplementary Discussion below).

Effect size: The deviation of each combinatorial perturbation from the prediction of the multiplicative model is represented as effect size, which was quantified in this case as absolute Cohen’s d, or the standardized deviation of the combinatorial phenotype from multiplicative model prediction.

Effect size = $| \mu_{\mathrm{obs}} - \mu_{\mathrm{pred}} | / \sigma_{\mathrm{pooled}}$

where μ_{obs} and μ_{pred} are the observed and predicted means for the combination effect and σ_{pooled} is the pooled standard deviation. In Fig. 3b, the cut-off for the effect size was 5.

Calculation of r-squared for multiplicative and linear fit models

R^2 values for coefficient of determination were calculated for each perturbation and cell-type readout (e.g., for Wnt3a perturbations on the #EdU$^+$ cells) as follows:

$R^2 = 1 - (SS_{res}/SS_{tot})$

SS_{res} = sum(actual effect - expected double perturbation effect)^2

SS_{tot} = sum (double perturbation effect - mean of all double perturbation effects for a given perturbation)^2

A negative R^2 value indicated that taking a mean of the double perturbation effects was a more reasonable predictive model than the multiplicative and/or linear fit models.

Signaling network visualization

Patterns of crosstalk between pathways were visualized using the networkx package in Python. Each perturbation was given as a node. Whether an edge existed between each pair of nodes was determined based on the cut-off of the effect size of the comparison between the observed double perturbation phenotype and the predicted multiplicative combination effect. Node sizes were determined based on the number of edges connecting to each node. The edge weights were determined based on the magnitude of the effect size.

BMP2 ELISA

Supernatant levels of BMP2 were quantified using a BMP-2 Quantikine ELISA kit (R&D Systems #DBP200), without significant deviations from manufacturer’s instructions.

RT-qPCR

RNA was harvested from enteroid monolayers using an RNEasy Plus Mini Kit (Qiagen #74136). Reverse transcription was performed using iScript Reverse Transcription kit (Bio-Rad #1708841). Quantitative PCR was performed using SsoAdvanced Universal SYBR Green Supermix (Bio-Rad #1725272) on a BioRad CFXConnect. Test gene values were normalized to beta- actin values. To quantify Atoh1/Hes1 ratio, both Atoh1 and Hes1 fold-changes relative to control were calculated and then Atoh1 fold-change was divided by Hes1 fold-change. RNA levels were determined using the following primers:

Target mRNA	Forward Primer	Reverse Primer
Atoh1	5'-TCCCCTTCCTCCTACCTTCTCC-3’	5'-CAACACGCAAGGATGAACTCCC-3’
Hes1	5’-AGAAGAGGCGAAGGGCAAGAAT-3’	5’-TGGAATGCCGGGAGCTATCTTT-3’
Smad7	5'-CCTCCTCCTTACTCCAGATACCC-3'	5'-CTGGGAGAAACCTGATGAAA-3'

Cdk6	5’-GGCGTACCCACAGAAACCATA-3’	5’-AGGTAAGGGCCATCTGAAAACT-3’
Bmp2	5'-GCTTCTTAGACGGACTGCGG-3'	5'-GCAACACTAGAAGACAGCGGGT-3'
beta-actin	5'-CGCCACCAGTTCGCCATGGA-3'	5'-TACAGCCCGGGGAGCATCGT-3'

Supplementary Discussion

Selecting readouts of progenitor proliferation and mature cell-fate specification

In many studies, perturbation effects are generally quantified by measuring changes in the expression of a cell-type marker gene relative to a housekeeping gene (e.g., changes in Muc2 RNA relative to β-actin RNA in an entire 3D organoid or crypt)[6]. Alternatively, large changes in the proportion of an organoid that is comprised of a given cell-type can be approximated in 3D organoids based on immunofluorescence images. These approaches are often taken rather than quantifying precise numbers of cell-types themselves because it is difficult to obtain accurate counts of many different cell-types in 3D organoids or *in vivo* due to the challenges of segmentation both in 3D and in tissues. However, multiple factors could give rise to any observed change in relative RNA expression or changes in the proportion of an organoid that is comprised of a given cell-type. For instance, a decrease in the relative expression of Muc2 RNA or the percentage of an organoid that stains positive for Muc2 may be caused by an increase in proliferation, a decrease in secretory cell specification, or a decrease in goblet cell specification within the secretory lineage. Here, we were able to distinguish these different possibilities because we measured several major progenitor and differentiated intestinal epithelial cell-types. Systematically measuring multiple cell-types also enabled us to combine numbers of individual cell-types to construct orthogonal readouts of two main tissue processes: proliferation and cell-fate specification, which we go into more detail on below.

Proliferation: Proliferation is a term synonymous with cell cycling or division. In the tissue context, proliferation is important for regeneration and production of sufficient numbers of cells to renew the tissue[48]. We quantified tissue proliferation by measuring the number of EdU$^+$ cells (in all cases in this work, in an entire well of enteroid monolayers). In the intestinal epithelium, >80% of cycling cells are in S phase at any given time[49], indicating that EdU staining will capture the vast majority of proliferating cells. We further subdivided the total EdU$^+$ cell population into EdU$^+$ stem cells and transit-amplifying cells based on the presence or absence of Lgr5 expression (stem and TA, respectively).

Cell-fate specification: Specification is the process by which differentiating cells adopt mature cell fates. We focus on two steps in the intestinal cell-fate specification: the split into secretory versus absorptive fates and the specification of goblet, Paneth, and enteroendocrine cell-types within the secretory fate. To measure the secretory-absorptive cell fate decision, we quantified the fraction of secretory cells (Muc2$^+$, Lyz$^+$, or ChgA$^+$) within differentiated cells (defined as Lgr5$^-$ and EdU$^-$ cells). To measure the specification of individual secretory cell-types, we measured the fractions of goblet (Muc2$^+$) cells, Paneth (Lyz$^+$) cells, and EE (ChgA$^+$) cells within the total secretory cell population (Muc2$^+$ + Lyz$^+$ + ChgA$^+$). There are other shared common progenitors during the cell-fate specification process that we do not quantify here. For instance, goblet and Paneth cells are thought to share a common progenitor, which may result in correlations between the goblet and Paneth cell fates within the secretory compartment[50]. Finally, we note that de-differentiation from a TA progenitor or differentiated cell type has been observed in the intestinal crypt under certain conditions[46,51,52]. We have not specifically observed this phenomenon in enteroid monolayer cultures but acknowledge that these processes may also contribute to the measured phenotypes.

Identifying perturbation crosstalk

To identify signaling pathway crosstalk, we first established a model for how perturbation effects should combine if there is no crosstalk. A simple model commonly used in genetic and drug interaction and crosstalk studies is the multiplicative model[53,54]. Under the multiplicative model, perturbations that have no crosstalk mechanisms should combine as the product of their respective fold-change effects. This is equivalent to log-additivity, which can be calculated as follows:

$$\log_2 fc(AB_{predicted}) = \log_2 fc(A_{obs}) + \log_2 fc(B_{obs})$$

Perturbation combination effects that deviate from the multiplicative model indicate potential crosstalk, which we define biologically as the due to utilization of a shared pathway or redundant pathways[21].

For each perturbation pair, we evaluated how a multiplicative model fits the observed double perturbation effects for each cell-type readout (e.g., #TA cells). To evaluate the multiplicative model for each perturbation and readout, we plotted the effects of perturbation combinations (e.g, the effects Wnt3a in combination with all other perturbations on proliferation) against the single perturbations (e.g., all perturbations except Wnt3a) in log scale. The multiplicative model prediction is a line offset on the y-axis by the effect of the perturbation of interest (Supplementary Fig. 6b). Combinations of perturbations that do not exhibit crosstalk will have an effect that lies on this line. We compared linear and multiplicative functions for each single perturbation and observed that some single perturbations fit well with either multiplicative or linear fit models, while others deviated significantly from both (e.g., Wnt3a fits well with either model while EGFR-i deviates significantly from both, see Supplementary Fig. 6b). We computed the residuals for perturbation combination fit across all readouts. The two models had similar distributions of residual values with peaks close to zero (Supplementary Fig. 6a), indicating that the majority of perturbations in our experiment combined in a manner that is well described by both linear-fit and multiplicative models. Overall, we observed similar r squared value distributions for each model (Supplementary Fig. 6c), indicating that the multiplicative model is a well-fitting linear model for the data. We did not observe a correlation between the magnitude of perturbation effects and deviation from either multiplicative or linear-fit models, eliminating a potential source of crosstalk false positives[55] (Supplementary Fig. 6d). We proceeded with the multiplicative model for identifying crosstalk between perturbations because it is more intuitive and because it successfully identified expected crosstalk between perturbations in the same pathway (Fig. 3, Supplementary Table 3).

References

1. Cheng, H. & Leblond, C. P. Origin, differentiation and renewal of the four main epithelial cell types in the mouse small intestine. V. Unitarian Theory of the origin of the four epithelial cell types. *Am. J. Anat.* **141**, 537–561 (1974).
2. Tian, A., Benchabane, H., Wang, Z. & Ahmed, Y. Regulation of Stem Cell Proliferation and Cell Fate Specification by Wingless/Wnt Signaling Gradients Enriched at Adult Intestinal Compartment Boundaries. *PLoS Genet.* **12**, e1005822 (2016).
3. Beumer, J. & Clevers, H. Regulation and plasticity of intestinal stem cells during homeostasis and regeneration. *Development* **143**, 3639–3649 (2016).
4. Thorne, C. A. *et al.* Enteroid Monolayers Reveal an Autonomous WNT and BMP Circuit Controlling Intestinal Epithelial Growth and Organization. *Dev. Cell* **44**, 624–633.e4 (2018).
5. Haber, A. L. *et al.* A single-cell survey of the small intestinal epithelium. *Nature* **551**, 333–339 (2017).
6. Yin, X. *et al.* Niche-independent high-purity cultures of Lgr5+ intestinal stem cells and their progeny. *Nat. Methods* **11**, 106–112 (2014).
7. von Moltke, J., Ji, M., Liang, H.-E. & Locksley, R. M. Tuft-cell-derived IL-25 regulates an intestinal ILC2–epithelial response circuit. *Nature* **529**, 221–225 (2015).
8. Basak, O. *et al.* Induced Quiescence of Lgr5+ Stem Cells in Intestinal Organoids Enables Differentiation of Hormone-Producing Enteroendocrine Cells. *Cell Stem Cell* **20**, 177–190.e4 (2017).
9. van Es, J. H. *et al.* Wnt signalling induces maturation of Paneth cells in intestinal crypts. *Nat. Cell Biol.* **7**, 381–386 (2005).
10. Qi, Z. *et al.* BMP restricts stemness of intestinal Lgr5 stem cells by directly suppressing their signature genes. *Nat. Commun.* **8**, 13824 (2017).
11. Batlle, E. *et al.* Beta-catenin and TCF mediate cell positioning in the intestinal epithelium by

controlling the expression of EphB/ephrinB. *Cell* **111**, 251–263 (2002).

12. Richmond, C. A. *et al.* JAK/STAT-1 Signaling Is Required for Reserve Intestinal Stem Cell Activation during Intestinal Regeneration Following Acute Inflammation. *Stem Cell Reports* **10**, 17–26 (2018).
13. van der Flier, L. G. & Clevers, H. Stem cells, self-renewal, and differentiation in the intestinal epithelium. *Annu. Rev. Physiol.* **71**, 241–260 (2009).
14. Houde, M. *et al.* Intestinal Epithelial Cell Differentiation Involves Activation of p38 Mitogen-activated Protein Kinase That Regulates the Homeobox Transcription Factor CDX2. *J. Biol. Chem.* **276**, 21885–21894 (2001).
15. Rodríguez-Colman, M. J. *et al.* Interplay between metabolic identities in the intestinal crypt supports stem cell function. *Nature* **543**, 424–427 (2017).
16. Stamataki, D. *et al.* Delta1 expression, cell cycle exit, and commitment to a specific secretory fate coincide within a few hours in the mouse intestinal stem cell system. *PLoS One* **6**, e24484 (2011).
17. Bjerknes, M. & Cheng, H. Clonal analysis of mouse intestinal epithelial progenitors. *Gastroenterology* **116**, 7–14 (1999).
18. Matsu-Ura, T. *et al.* Intercellular Coupling of the Cell Cycle and Circadian Clock in Adult Stem Cell Culture. *Mol. Cell* **64**, 900–912 (2016).
19. Garabedian, E. M., Roberts, L. J., McNevin, M. S. & Gordon, J. I. Examining the role of Paneth cells in the small intestine by lineage ablation in transgenic mice. *J. Biol. Chem.* **272**, 23729–23740 (1997).
20. Deng, H., Gerencser, A. A. & Jasper, H. Signal integration by Ca2 regulates intestinal stem-cell activity. *Nature* **528**, 212–217 (2015).
21. Dixon, S. J., Costanzo, M., Baryshnikova, A., Andrews, B. & Boone, C. Systematic mapping of genetic interaction networks. *Annu. Rev. Genet.* **43**, 601–625 (2009).
22. Kampmann, M., Bassik, M. C. & Weissman, J. S. Functional genomics platform for pooled screening and generation of mammalian genetic interaction maps. *Nat. Protoc.* **9**, 1825–1847 (2014).

23. Bassik, M. C. *et al.* A systematic mammalian genetic interaction map reveals pathways underlying ricin susceptibility. *Cell* **152**, 909–922 (2013).
24. Papin, J. A., Hunter, T., Palsson, B. O. & Subramaniam, S. Reconstruction of cellular signalling networks and analysis of their properties. *Nat. Rev. Mol. Cell Biol.* **6**, 99–111 (2005).
25. Coster, A. D., Thorne, C. A., Wu, L. F. & Altschuler, S. J. Examining Crosstalk among Transforming Growth Factor β, Bone Morphogenetic Protein, and Wnt Pathways. *J. Biol. Chem.* **292**, 244–250 (2017).
26. Goldman, D. C., Donley, N. & Christian, J. L. Genetic interaction between Bmp2 and Bmp4 reveals shared functions during multiple aspects of mouse organogenesis. *Mech. Dev.* **126**, 117–127 (2009).
27. Podolsky, D. K. Regulation of intestinal epithelial proliferation: a few answers, many questions. *American Journal of Physiology-Gastrointestinal and Liver Physiology* **264**, G179–G186 (1993).
28. Birchenough, G. M. H., Nyström, E. E. L., Johansson, M. E. V. & Hansson, G. C. A sentinel goblet cell guards the colonic crypt by triggering Nlrp6-dependent Muc2 secretion. *Science* **352**, 1535–1542 (2016).
29. Grinenko, T. *et al.* Hematopoietic stem cells can differentiate into restricted myeloid progenitors before cell division in mice. *Nat. Commun.* **9**, 1898 (2018).
30. Cheng, H. & Leblond, C. P. Origin, differentiation and renewal of the four main epithelial cell types in the mouse small intestine. I. Columnar cell. *Am. J. Anat.* **141**, 461–479 (1974).
31. Clevers, H. The Intestinal Crypt, A Prototype Stem Cell Compartment. *Cell* **154**, 274–284 (2013).
32. Farin, H. F. *et al.* Visualization of a short-range Wnt gradient in the intestinal stem-cell niche. *Nature* **530**, 340–343 (2016).
33. Li, Y. *et al.* A growth factor-free culture system underscores the coordination between Wnt and BMP signaling in Lgr5 intestinal stem cell maintenance. *Cell Discov* **4**, 49 (2018).
34. van der Flier, L. G., Haegebarth, A., Stange, D. E., van de Wetering, M. & Clevers, H. OLFM4 is a robust marker for stem cells in human intestine and marks a subset of colorectal cancer cells. *Gastroenterology* **137**, 15–17 (2009).

35. Flentjar, N. *et al.* TGF-betaRII rescues development of small intestinal epithelial cells in Elf3-deficient mice. *Gastroenterology* **132**, 1410–1419 (2007).
36. Han, L. *et al.* The Notch pathway inhibits TGFβ signaling in breast cancer through HEYL-mediated crosstalk. *Cancer Res.* **74**, 6509–6518 (2014).
37. Hong, S. P. *et al.* Generation of PDGFRα Cardioblasts from Pluripotent Stem Cells. *Sci. Rep.* **7**, 41840 (2017).
38. VanDussen, K. L. *et al.* Notch signaling modulates proliferation and differentiation of intestinal crypt base columnar stem cells. *Development* **139**, 488–497 (2012).
39. Dames, P. *et al.* Interleukin-13 affects the epithelial sodium channel in the intestine by coordinated modulation of STAT6 and p38 MAPK activity. *J. Physiol.* **593**, 5269–5282 (2015).
40. Houde, M. *et al.* Intestinal epithelial cell differentiation involves activation of p38 mitogen-activated protein kinase that regulates the homeobox transcription factor CDX2. *J. Biol. Chem.* **276**, 21885–21894 (2001).
41. Sato, T. *et al.* Long-term expansion of epithelial organoids from human colon, adenoma, adenocarcinoma, and Barrett’s epithelium. *Gastroenterology* **141**, 1762–1772 (2011).
42. Tian, H. *et al.* A reserve stem cell population in small intestine renders Lgr5-positive cells dispensable. *Nature* **478**, 255–259 (2011).
43. Sato, T. *et al.* Single Lgr5 stem cells build crypt-villus structures in vitro without a mesenchymal niche. *Nature* **459**, 262–265 (2009).
44. Salic, A. & Mitchison, T. J. A chemical method for fast and sensitive detection of DNA synthesis in vivo. *Proceedings of the National Academy of Sciences* **105**, 2415–2420 (2008).
45. Ramirez, M. *et al.* Diverse drug-resistance mechanisms can emerge from drug-tolerant cancer persister cells. *Nat. Commun.* **7**, 10690 (2016).
46. van Es, J. H. *et al.* Dll1+ secretory progenitor cells revert to stem cells upon crypt damage. *Nat. Cell Biol.* **14**, 1099–1104 (2012).
47. Potten, C. S. Stem cells in gastrointestinal epithelium: numbers, characteristics and death. *Philos.*

Trans. R. Soc. Lond. B Biol. Sci. **353**, 821–830 (1998).

48. Potten, C. S. & Loeffler, M. Stem cells: attributes, cycles, spirals, pitfalls and uncertainties. Lessons for and from the crypt. *Development* **110**, 1001–1020 (1990).
49. Carroll, T. D., Newton, I. P., Chen, Y., Julian Blow, J. & Näthke, I. Lgr5 intestinal stem cells reside in an unlicensed G1 phase. *J. Cell Biol.* **217**, 1667–1685 (2018).
50. Shroyer, N. F., Wallis, D., Venken, K. J. T., Bellen, H. J. & Zoghbi, H. Y. Gfi1 functions downstream of Math1 to control intestinal secretory cell subtype allocation and differentiation. *Genes Dev.* **19**, 2412–2417 (2005).
51. Tetteh, P. W. *et al.* Replacement of Lost Lgr5-Positive Stem Cells through Plasticity of Their Enterocyte-Lineage Daughters. *Cell Stem Cell* **18**, 203–213 (2016).
52. Buczacki, S. J. A. *et al.* Intestinal label-retaining cells are secretory precursors expressing Lgr5. *Nature* **495**, 65–69 (2013).
53. van Hasselt, J. G. C. & Iyengar, R. Systems Pharmacology: Defining the Interactions of Drug Combinations. *Annu. Rev. Pharmacol. Toxicol.* **59**, 21–40 (2019).
54. Mani, R., St Onge, R. P., Hartman, J. L., 4th, Giaever, G. & Roth, F. P. Defining genetic interaction. *Proc. Natl. Acad. Sci. U. S. A.* **105**, 3461–3466 (2008).
55. Horlbeck, M. A. *et al.* Mapping the Genetic Landscape of Human Cells. *Cell* **174**, 953–967.e22 (2018).